Examining Willman 1,
an enigmatic Milky Way satellite

The Astrophysical Journal, 1002:55 (18pp), 2026 April 20 https://doi.org/10.3847/1538-4357/ae4a2a

~~Willman 1 Revisited: The Kinematics, Chemistry, and Orbital Properties of a Potentially Disrupting Dwarf Galaxy~~

Me! :)

Camille Chiu[1], Marla Geha[1], William Cerny[1], Nitya Kallivayalil[2], Hannah Richstein[2], Christopher T. Garling[2], and Beth Willman[3]

[1] Department of Astronomy, Yale University, New Haven, CT 06520, USA; camille.chiu@yale.edu
[2] Department of Astronomy, University of Virginia, Charlottesville, VA 22904, USA
[3] LSST Discovery Alliance, 933 North Cherry Avenue, Tucson, AZ 85719, USA

My wonderful mentor throughout my undergraduate research career!

Received 2025 December 15; revised 2026 February 20; accepted 2026 February 20; published 2026 April 24

Who Willman 1 is named after!

Abstract

The ultra-faint Milky Way satellite Willman 1 (W1; $M_V = -2.6$; $r_{\rm half} \sim 27$ pc) was the first stellar overdensity found [illegible] stars in the Sloan Digital Sky Survey, yet its classification as a dwarf galaxy or star cluster remains ambiguous. Using new Keck/DEIMOS spectroscopy, Hubble Space Telescope photometry, and orbital modeling, we re-examine the nature of W1. From our updated member sample of 56 stars, we find that past analyses included four binaries and seven nonmembers, identified using Gaia proper motions and updated velocities. We continue to find a velocity dispersion consistent with previous analyses, measuring $\sigma_v = 4.7^{+1.5}_{-1.3}$ km s^{-1} from 49 stars out to 3 $r_{\rm half}$. If W1 is in equilibrium, this suggests a dynamical mass of $5.9^{+3.7}_{-3.4} \times 10^5 M_\odot$ and mass-to-light ratio of $(M/L)_V = 660 \pm 590$. Based on Ca II triplet measurements, we estimate an iron abundance of $[{\rm Fe/H}] = -2.45^{+0.12}_{-0.13}$ and a metallicity dispersion of $\sigma_{\rm [Fe/H]} = 0.20^{+0.15}_{-0.11}$ dex. We find that W1 does not show mass segregation inside $\sim 1\, r_{\rm half}$. Our best-fit orbital model predicts that W1 is at apocenter, implying that W1 has been closer to the Milky Way in the recent past with a pericentric passage $\lesssim 25$ kpc from the Galactic center ~ 0.5 Gyr ago. Given its internal kinematics, metallicity spread, and lack of mass segregation, we conclude that W1 is a galaxy. However, given its orbit and structural properties, which suggest that W1 might be tidally disrupted, as well as the difficulty in identifying a pure member sample, we caution that the measured internal velocity dispersion may not accurately reflect [illegible] of the system.

TLDR:

Willman 1 is a small, faint grouping of stars that orbits the Milky Way. Although discovered 20 years ago, the nature of this object remains ambiguous even today. This work uses observations from the Keck II telescope, the *Gaia* space satellite, and the *Hubble Space Telescope* to answer two fundamental questions about the nature of this object:

(1) Is Willman 1 a dwarf galaxy or a star cluster? (galaxy!)
(2) Is Willman 1 in dynamical equilibrium? (probably not …)

Unified Astronomy Thesaurus concepts: Dwarf galaxies (416); Stellar kinematics (1608); Milky Way dynamics (1051)

Materials only available in the online version of record: machine-readable table

Background:

1. Introduction

The advent of wide-field photometric surveys such as the Sloan Digital Sky Survey (SDSS) and the Dark Energy Survey (DES) has led to the rapid discovery of several dozen Milky Way satellite galaxies, including populations of ultra-faint dwarf galaxies and ultra-faint star clusters (e.g., B. Willman et al. 2005; V. Belokurov et al. 2007; A. Drlica-Wagner et al. 2015; S. E. Koposov et al. 2015; G. Torrealba et al. 2016; W. Cerny et al. 2024; D. Homma et al. 2024). The faintest and most compact of these stellar systems, with stellar masses of only a few hundred solar masses and half-light radii of a few tens of parsecs, blur the line between star clusters and galaxies (e.g., S. E. T. Smith et al. 2024). The classification of an object as a dwarf galaxy or star cluster typically hinges on one or both of the following diagnostics (B. Willman & J. Strader 2012): (1) a kinematic distribution that cannot be explained solely by its baryonic component, implying the presence of large quantities of dark matter; (2) a spectroscopically observed spread in [Fe/H] metallicity, indicating multiple epochs of star formation. Beyond these two criteria, the presence of mass segregation has also been proposed as a discriminator (H. Baumgardt et al. 2022).

One such system that straddles the boundary between dwarf galaxies and star clusters is the Milky Way satellite Willman 1 (W1; SDSSJ1049+5103). W1 was first identified as an overdensity of old, metal-poor stars in SDSS DR2 by B. Willman et al. (2005) and was the lowest-luminosity galaxy known at the time of discovery ($M_V = -2.5$; B. Willman et al. 2005). Despite tentative evidence for mass segregation, B. Willman et al. (2006) initially leaned toward a dwarf galaxy classification for W1 based on an observed metallicity spread between three red giant branch (RGB) stars. This classification was supported by Keck/DEIMOS spectroscopy by N. F. Martin et al. (2007), who identified seven RGB members with a significant metallicity spread. However, follow-up spectroscopy from the Hobby–Eberly Telescope by M. H. Siegel et al. (2008) determined that at least two and up to five of these identified RGB stars were likely Milky Way foreground dwarf stars, significantly decreasing the observed metallicity spread. From an analysis with Keck/DEIMOS spectroscopy and a careful characterization of foreground contamination, B. Willman et al. (2011) identified 45 member stars, 40 of which were classified at high confidence. This included an additional RGB member and two horizontal branch members whose metallicity spread was once again indicative of a dwarf galaxy. These spectroscopic results are supported by the photometric Hubble Space Telescope (HST)-based metallicity distribution function measured by S. W. Fu et al. (2023), who determined a significant metallicity spread of $\sigma_{\rm [Fe/H]} = 0.65^{+0.10}_{-0.09}$ dex.

Just as many planets in our Solar System are surrounded by smaller moons, our own Milky Way galaxy is orbited by smaller satellite galaxies, aptly named dwarf galaxies.

Willman 1 (W1) was the first ultra-faint dwarf galaxy candidate discovered in 2005. However, since it is so faint and compact, it is difficult to tell whether this object is a galaxy or a star cluster …

Here are some properties that can be used to differentiate between these two types of objects:

Star clusters vs. dwarf galaxies

No dark matter	Lotsss of dark matter
All stars have similar chemical compositions	Stars have different chemical compositions
Mass segregation	No mass segregation

Star clusters form all their stars at the same time while dwarf galaxies undergo multiple cycles of star formation, each successively containing more metals.

Dwarf galaxies are the most dark matter dominated objects known in the Universe!

Over time, high-mass stars sink towards the center of the system while low-mass stars drift to the outskirts, hence the term mass segregation. The massive amounts of dark matter in dwarf galaxies extend the timescale of this process beyond the age of the Universe!

The results of follow-up observations of Willman I in 2006, 2007, 2008, and 2011 oscillated between a dwarf galaxy and a star cluster classification. If Willman I is a dwarf galaxy, it is one of the most promising targets in the search for radiation signals from theorized dark matter particles.

However, these studies also raised concerns that Willman I might not be in dynamical equilibrium, but instead perturbed by its proximity to the Milky Way. This is crucial because the techniques we use to infer the mass of gravitationally bound objects such as Willman I assume that its stars are in dynamical equilibrium.

In this work, we use 20 years of archival data from the Keck II telescope, data from the *Gaia* space telescope, and data from the *Hubble Space Telescope* to probe the nature of Willman I!

Assuming equilibrium, B. Willman et al. (2011) estimated the dynamical mass of W1 to be $\sim 3.9 \times 10^5 M_\odot$ based on a velocity dispersion of 4.8 ± 0.8 km s^{-1}, implying a mass-to-light ratio of ~ 770. Due to this purported high dark matter content and relatively close proximity at a distance of ∼39 kpc, W1 remains one of the most promising targets in the search for dark matter annihilation signals in gamma-rays (e.g., E. Aliu et al. 2009; T. Bringmann et al. 2009; S. Li et al. 2021; A. McDaniel et al. 2023) and X-rays (e.g., D. Nieto & N. Mirabal 2010, M. Loewenstein & A. Kusenko 2010, 2012, S. Saeedi & M. Sasaki 2020).

Yet, previous studies of W1 found evidence for dynamical disequilibrium, including stellar multidirectional tails and a tentative excess of stars at large half-light radii (B. Willman et al. 2006, 2011). Specifically, B. Willman et al. (2011) reported an irregular kinematic distribution where stars within the effective half-light radius have a systematically higher velocity than those [illegible] might point to tidal interactions. If W1 is not in dynamical equilibrium and indeed is undergoing tidal disruption, then the dynamical mass inferred from its internal velocity dispersion may be misleading.

The main difficulty in accurately classifying W1 and determining its properties lies in the kinematic and spectroscopic similarities between the foreground stars in the Milky Way and the members of W1 (M. H. Siegel et al. 2008; B. Willman et al. 2011; S. Saeedi & M. Sasaki 2020). With an estimated systemic radial velocity of -12.8 ± 1.0 km s^{-1}, the velocities of W1 stars substantially overlap [illegible] of Milky Way stars (B. Willman et al. 2011). If W1 is dynamically disturbed, spatial and kinematic [illegible] often implemented to supplement photometric color-magnitude diagram (CMD) cuts, might instead obscure the odd structural and kinematic features of W1. On the other hand, due to the already small sample size of stars, just a few Milky Way contaminants in the member sample could artificially alter the velocity dispersion and, thus, the inferred dynamical mass of W1, as well as the metallicity spread that is used to characterize it as a dwarf galaxy in the first place.

To address these uncertainties, this paper revisits W1 and presents a comprehensive study of its structural, kinematic, chemical, and orbital properties. First, we describe our uniform analysis of both new and archival Keck/DEIMOS spectroscopy for W1 and our incorporation of Gaia astrometry (Section 2). We then discuss the probabilistic membership selection performed to reduce the presence of Milky Way foreground contamination (Section 3). From this member sample, we measure the properties of W1 including its velocity dispersion, inferred dynamical mass, and metallicity distribution (Section 4). With HST/Advanced Camera for Surveys (ACS) imaging of W1, we summarize previous results for W1's star formation history and look for evidence of mass segregation (Section 5). We next model the orbital history of W1 and simulate mock tidal streams (Section 6). We conclude with a discussion of W1's classification as either a dwarf galaxy or star cluster and its tidal disruption status (Section 7).

2. Observations and Data Reduction

Our kinematic and metallicity analysis is based on a homogeneous reduction of archival Keck/DEIMOS spectroscopic data (Sections 2.1 and 2.2), half of which are published here for the first time. We supplement this with ground-based photometry and Gaia astrometry (Section 2.3).

2.1. Keck/DEIMOS Spectroscopy: Kinematics

We present homogeneously reduced archival data of W1 from the DEIMOS spectrograph (S. M. Faber 2003) on the Keck II 10 m telescope. Twelve multislit masks were taken of W1 between 2006 and 2025 (see Table 1). One of these masks was first presented in N. F. Martin et al. (PI: Chapman 2007), and four masks were published in B. Willman et al. (PI: Brodie 2011). The remaining seven masks are presented here for the first time [PIs: Geha, Rich]. All data were taken with the 1200G grating, providing a spectral resolving power of $R \sim 6000$ at 8500 Å. The spectral dispersion of this setup is roughly 0.33 Å per pixel with a resulting spectral resolution of 1.37 Å (FWHM). A summary of observations is presented in Table 1.

A detailed discussion of the data reduction is presented in M. Geha et al. (2026) and briefly discussed here. Raw science frames and associated calibrations were obtain through the Keck Observatory Archive.[4] Data were reduced to one-dimensional wavelength-calibrated spectra using the open-source python-based data reduction code `PypeIt` (J. X. Prochaska et al. 2020). `PypeIt` reduces the eight individual DEIMOS detectors as four mosaic images, where each red/blue pair of detectors is reduced together.

Stellar radial velocities were measured using the `dmost` package (M. Geha et al. 2026).[5] `dmost` first pre-processes spectra to identify and remove extragalactic objects using a modified version of the automated redshift software `Marz` (S. R. Hinton et al. 2016). For the remaining spectra, `dmost` forward models the one-dimensional spectrum for each source from a given exposure with both a stellar template from the PHOENIX library (T. O. Husser et al. 2013) and a synthetic telluric absorption spectrum from TelFit (K. Gullikson et al. 2014). The velocity is determined for each science exposure through a Markov Chain Monte Carlo (MCMC) procedure determining both [illegible] as well as a wavelength shift of the telluric spectrum needed to correct for slit miscentering (see, e.g., S. T. Sohn et al. 2007). We reject velocities where the posterior shapes is far from Gaussian, largely spectra with signal-to-noise ratio (S/N) <3. The final radial velocity for each star is derived through an inverse-variance weighted average of the velocity measurements from each individual exposure. In cases where less than half of individual science exposures for a given star produce a reliable velocity measurement, we attempt to measure a velocity based on the one-dimensional coadded spectrum following the same method above. In both cases, a velocity error floor is applied to the random errors, based on an assessment from thousands of repeat DEIMOS measurements as discussed in M. Geha et al. (2026). The velocity error floor is 1.1 km s^{-1} for a velocity measured on a single mask.

There are 474 unique targets with extracted DEIMOS spectra plus 28 sources extracted serendipitously in addition to the target source. We have photometry and were able to measure radial velocities for 340 of these sources. We find that 125 of these sources are extragalactic including 14 broad-line

---

[4] https://koa.ipac.caltech.edu

[5] https://github.com/marlageha/dmost

Data:

Table 1
Summary of Willman 1 Keck/DEIMOS Observations

Mask	Date	N_{exp}	Σt_{exp} (sec)	PIs	Slit Width (arcsec)	N_{slits}	N_{good}/N_{slits}	References
203WiSB	20060527	3	3600	Chapman	0.7	63	0.62	N. F. Martin et al. (2007)
W1_1	20061120	5	9000	Brodie	1.0	113	0.48	B. Willman et al. (2011)
W1_2	20061121	5	[illegible]	[illegible]	[illegible]	[illegible]	[illegible]	B. Willman et al. (2011)
W1_3	20061122	3	5400	Brodie	1.0	92	0.41	B. Willman et al. (2011)
W1_4	20070320	3	[illegible]	Brodie	[illegible]	[illegible]	0.07	B. Willman et al. (2011)
W1_5	20170425	7	12000	Geha	0.7	71	0.28	New Data; this work
W1_6	20170426	5	9000	Geha	0.7	66	0.42	New Data; this work
W1_9	20210408	5	9000	Geha	0.7	70	0.4	New Data; this work
Wil1_1B	20230124	6	7200	Rich	0.8	39	0.38	New Data; this work
wil1_5	20230124	6	7200	Rich	0.8	33	0.45	New Data; this work
Wil1_2B	20230125	6	7200	Rich	0.8	31	0.42	New Data; this work
wil1_6	20230125	6	7200	Rich	0.8	29	0.34	New Data; this work

Note. List of DEIMOS masks present in this work: (1) DEIMOS mask name, (2) date observed, (3) number of exposures reduced in this work, (4) total integrated exposure time, (5) Principal Investigator (PI) name, (6) slit width, (7) number of slits in a mask, (8) fraction of targeted objects in a mask with a measured velocity, and (9) published reference.

A table of all the archival observations from the Keck II Telescope we use, spanning from 2006 to 2023. The data from 2017 onward have never been published before!

This work is part of a larger project spearheaded by Prof. Marla Geha. The premise is this: Many different groups of astrophysicists have observed various Milky Way satellites on the Keck II telescope over the last few decades. However, each time, the data are reduced according to different methods.

Going from raw observations from a telescope (like those shown on the right) to measurements of stars' properties (position, velocity, metallicity, etc.), which involves a lot of precise statistics

quasar spectra. The remaining 215 sources have velocities and spectra consistent with stars, although we expect only a fraction of these to be W1 members (see Section 3.1). We note that 12 of these sources have velocity uncertainties >15 km s^{-1}, above the threshold considered as a secure velocity measurement by M. Geha et al. (2026), and they are thus not considered for membership. We therefore consider 203 stars with measured radial velocities for membership. The radial velocities for the 203 stars and redshifts for the 125 extragalactic sources are available in Table A3 and A4 of M. Geha et al. (2026), respectively.

2.1.1. Flagging Velocity Variables

The orbital motions of unresolved binary star systems when measured at a single epoch can inflate a system's inferred velocity dispersion. To identify such velocity variable stars, we evaluate whether velocities measured at different times are consistent with random fluctuations from a constant value. For each star, we first calculate the weighted mean velocity, the equivalent of assuming a constant velocity model. We then calculate the χ^2 value for this model, including random and systematic error components. Following P. F. L. Maxted et al. (2001), we then calculate the probability, p, of obtaining the observed value of χ^2 or higher from random fluctuations around a constant value. p is evaluated for the appropriate number of degrees of freedom (the number of observations minus one). We define a star as a velocity variable if $\log_{10}p < -1$. Of the 340 stars with measured velocities, 63 have measurements on multiple DEIMOS mask pointings separated by more than one year. We find 16 of these stars to be velocity variables, six of which are members. Their positions on the CMD are shown in Figure 1(a).

2.2. Keck/DEIMOS Spectroscopy Metallicities

We use dmost to measure the equivalent width of several stellar absorption lines. We first determine equivalent widths for NaI: λ8183, 8185 Å and MgI: λ8807 Å. The strengths of the NaI and MgI lines are used as proxies for surface gravity to evaluate membership in W1. We model these lines as a double or single Gaussian, respectively, and integrate the resulting fitted parameters to determine equivalent widths.

These quantities are used at the end of Section 3.1 to validate membership selection.

We measure the equivalent width of the Ca II triplet (CaT) lines (λ8498, 8542, 8662 Å) as described in M. Geha et al. (2026). We simultaneously model the CaT lines with a Gaussian-plus-Lorentzian profile (for stars at S/N > 15 per spectral pixel) or a Gaussian profile (for stars at S/N < 15 per spectral pixel). We integrate the resulting fits to determine total equivalent width, which we refer to as CaT EW. From these CaT EW measurements, we derive [Fe/H] measurements for all candidate RGB stars ($M_V < 3$) assuming the empirical luminosity-depende [illegible] et al. (2026), which [illegible] calibration using th [illegible] of the calibration [illegible] ch w [illegible] band pho [illegible] M. Geha et al. (202 [illegible] CaT measurements [illegible] 0.1 dex error floor [illegible] for inherent scatter [illegible] this term dominate [illegible]

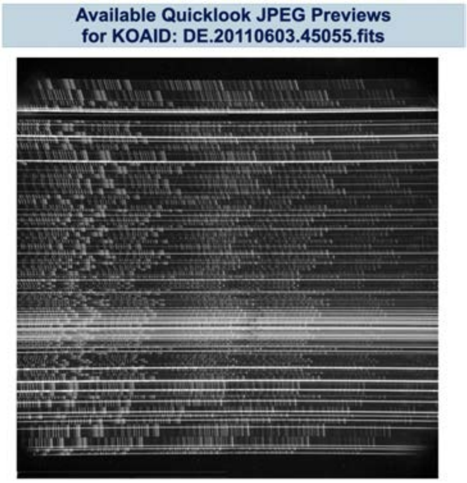
Available Quicklook JPEG Previews for KOAID: DE.20110603.45055.fits

2.3. Ground-[illegible]

We require phot [illegible] assess membership [illegible] Canada–France–Ha [illegible] metric catalog from R. R. Muñoz et al. (2018a) and adopt the fitted density profile and structural parameters from this analysis (see Table 2). These data are a full magnitude deeper than those available from the DESI Legacy Imaging Surveys DR9 (A. Dey et al. 2019). The R. R. Muñoz et al. (2018a) g- and r-band magnitudes are corrected for foreground Galactic extinction using D. J. Schlegel et al. (1998). Given the small magnitude uncertainties reported by R. R. Muñoz et al. (2018a, <0.01 mag), we add a systematic photometric uncertainty of 0.02 mag in quadrature.

A important improvement to previous studies of W1 is the available Gaia DR3 catalog (Gaia Collaboration et al. 2023). While Gaia will only cover W1 stars above the subgiant branch ($r \lesssim 20$), it significantly reduces contamination in this region due to the addition of proper-motion and parallax

Her work takes 20 years of archival data and reduces them all according to the same methods. This results in 22,339 stars in 78 Milky Way dwarf galaxies and star clusters whose properties are all homogeneously measured. The satellite Willman I deserves its own paper because it is such a weird object!

Membership:

When we observe an object in the sky, we not only see the stars in that object, but also all the stars in the Milky Way between us and that object. This means that the first step in studying Willman I is to discern which stars we have observed are actually a part of Willman I.

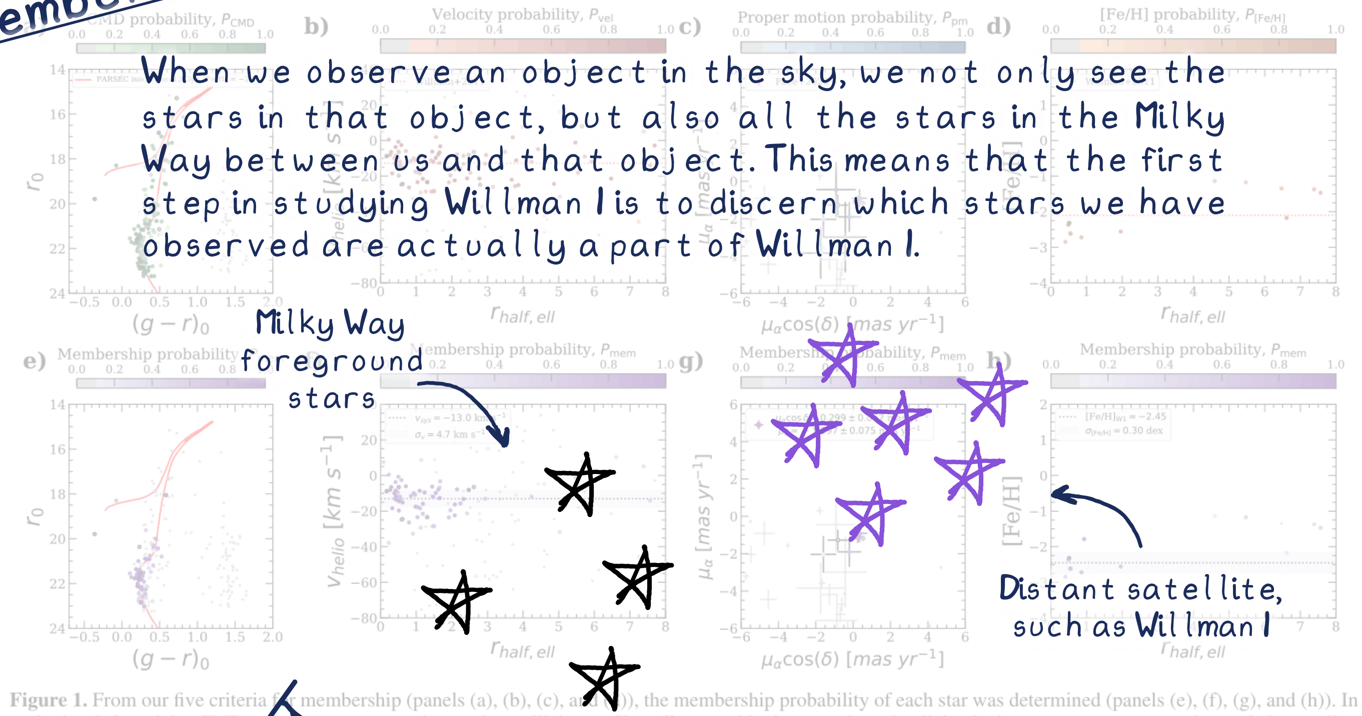

Milky Way foreground stars

Distant satellite, such as Willman I

Us!

Figure 1. From our five criteria for membership (panels (a), (b), (c), and (d)), the membership probability of each star was determined (panels (e), (f), (g), and (h)). In each plot (left to right: CMD, velocity, proper motion, and metallicity profile), all stars with photometric and radial velocity measurements are color-coded according to the membership probability of the criterion in question, with clear nonmembers ($P_{\rm criterion} < 0.1$) colored gray. Stars with variable velocities are circled in black. The priors for each marker are delineated in the top panels (A. B. Pace et al. 2022; B. Willman et al. 2011), and the properties derived from our member sample are shown in the bottom panels (see Section 4, Table 2).

However, especially for faint stars, we are often unable to measure the distances to them. This means that we need to find another way to differentiate between Milky Way stars and the member stars of Willman I ... mainly by looking at the velocities of the stars! All member stars should be moving towards or away from us at roughly the same speed, traveling together as a group.

measurements. We match our DEIMOS catalog to Gaia DR3 with a 1.″5 matching radius, resulting in 65 matches that are considered for membership.

3. Membership Sample

Assessing whether a given star belongs to W1 or is part of the foreground Milky Way is particularly challenging because of the kinematic overlap between these two populations. We begin by describing our membership assessment method (Section 3.1). We then present our final member sample and compare to previous member samples in the literature (Section 3.2).

3.1. Membership Determination

To evaluate the likelihood that a given star is a member of W1, we assess five criteria for membership: (1) the star's position on the CMD, $P_{\rm CMD}$; (2) the star's heliocentric radial velocity, $P_{\rm vel}$; (3) the star's proper motion, $P_{\rm pm}$; (4) the star's parallax, $P_{\rm parallax}$; and (5) the star's [Fe/H] iron abundance, $P_{\rm [Fe/H]}$. Criteria (3) and (4) are only considered for stars with parallax and proper motion measurements available from Gaia DR3 (Gaia Collaboration et al. 2023; see also Section 2.3).

Due to tentative evidence for multidirectional tails and tidal stripping (N. F. Martin et al. 2007; B. Willman et al. 2011), no spatial cuts were performed on the data so as to not introduce assumptions about W1's spatial spread of stars, although we limit our sample to 3 $r_{\rm half,ell}$ to determine physical properties (see Section 4). We additionally consider two surface gravity indicators (NaI and MgI), but find these do not improve membership discrimination for the case of W1 and discuss this below. The membership probability, $P_{\rm mem}$, of a star is defined as the product of all five criteria (Figure 1):

$$P_{\rm mem} \propto P_{\rm CMD} \times P_{\rm vel} \times P_{\rm pm} \times P_{\rm parallax} \times P_{\rm [Fe/H]}. \quad (1)$$

We next describe in more detail each of these terms.

$P_{\rm CMD}$ is determined by comparing each star's position on the [illegible] isochrone from the PARSEC stellar evolutionary track models ($\tau = 12$ Gyr, Fe/H $= -2.1$, A. Bressan et al. 2012). We use the updated distance value of 38.55 ± 0.45 kpc based on HST imaging from M. J. Durbin et al. (2025, uncertainty via private communication). This value is consistent with that measured in B. Willman et al. (2011), 38 ± 7 kpc. We use this to calculate the minimum distance between the isochrone and the star's location on the CMD. This distance ($d_{\rm min}$) and the overall magnitude uncertainty of the [illegible] quadrature sum of the r-band and g-band magnitude uncertainty), are then used to evaluate the star's CMD membership probability, $P_{\rm CMD}$ (see Figure 1(a)):

$$P_{\rm CMD} = \exp\left(-\frac{d_{\rm min}^2}{2[\sigma_{\rm CMD}^2 + \delta_{\rm mag}^2]}\right), \quad (2)$$

where $\sigma_{\rm CMD}$ is set to 0.15 mag. This CMD spread was estimated from the span of other possible isochrones with varying ages and metallicities ($\tau = 8$ to 13 Gyr, [Fe/H] $= -1.9$ to -2.3) to account for the uncertainty in both parameters.

$P_{\rm vel}$ is based on each star's heliocentric, line-of-sight velocity and, for consistency's sake, is calculated using a similar probability distribution as $P_{\rm CMD}$. For a star with velocity $v \pm \delta_v$, its membership probability based on velocity

Positions:

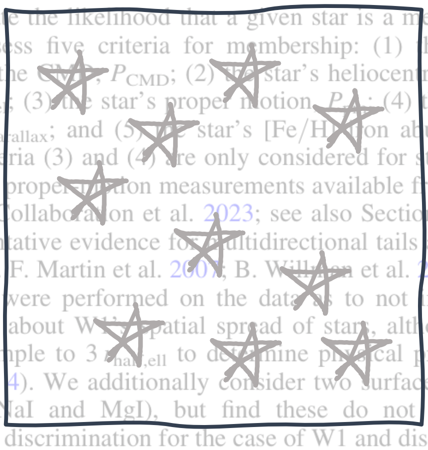

Unclear which stars we see are in Willman I

Velocities:

All Willman I members move together!

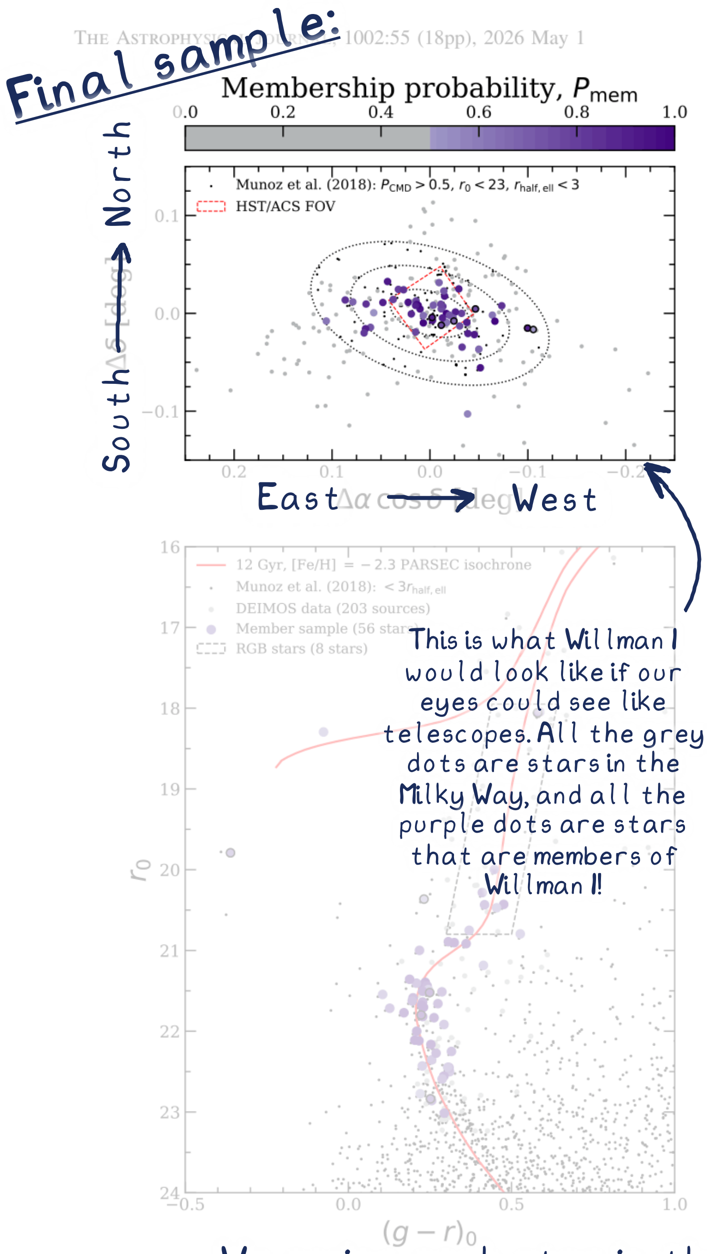

This is what Willman I would look like if our eyes could see like telescopes. All the grey dots are stars in the Milky Way, and all the purple dots are stars that are members of Willman I!

Figure 2. Top panel: Spatial distribution of the 56 W1 member stars, color-coded according to $P_{\rm mem}$. Members with variable velocities are circled in black, and nonmembers are colored in gray. The three concentric dotted ellipses represent the space within 1, 2, and 3 $r_{\rm half,ell}$. All stars with photometry from R. R. Muñoz et al. (2018a) within 3 $r_{\rm half,ell}$, $P_{\rm CMD} > 0.5$, and $r_0 < 23$ are shown in black. The field of view of the HST/ACS imaging is denoted red (see Section 5.1). Bottom panel: CMD of W1 member stars overlaid with an old, metal-poor PARSEC isochrone in red. All stars with photometry from R. R. Muñoz et al. (2018a) within 3 $r_{\rm half,ell}$ are shown in black. The liberally defined red giant branch (RGB) for which we measure spectroscopic metallicities is boxed.

We assign each star in the field of view of Willman I a membership probability that denotes how likely it is to be a part of Willman I based on its velocity and a few other factors.

Using this as a benchmark, we identify a <u>member sample of 56 stars</u>! Six of these stars are likely unresolved binaries and one is near the outskirts, so we opt to only use the remaining 49 stars to measure the properties of Willman I.

These are two stars orbiting around each other close enough that we observe them as one star with our telescopes. Observing two stars as one star makes for some wonky properties, so we don't include them in our analysis.

$P_{\rm vel}$, is calculated as (see Figure 1(b)):

$$P_{\rm vel} = \exp\left(-\frac{(v - v_{\rm W1})^2}{2[(3\sigma_v)^2 + \delta_v^2]}\right), \tag{3}$$

where $v_{\rm W1} = -12.8$ km s^{-1}, the systemic velocity of W1, and $\sigma_v = 4.8$ km s^{-1}, the velocity dispersion of W1, as determined by B. Willman et al. (2011). We multiply the velocity dispersion by 3 to loosen the distribution and avoid artificially biasing the sample toward the priors.

Table 2
Properties of Willman 1

Parameter	Value	Units	References
α_{J2000}	162.3436	deg	R. R. Muñoz et al. (2018a)
δ_{J2000}	51.0501	deg	R. R. Muñoz et al. (2018a)
$D_\odot$	38.55 ± 0.45	kpc	M. J. Durbin et al. (2025)[a]
$(m-M)_0$	17.93 ± 0.03	mag	M. J. Durbin et al. (2025)[a]
$r_{\rm half}$	2.51 ± 0.22	arcmin	R. R. Muñoz et al. (2018b)
$r_{\rm half}$	26.8 ± 3.2	pc	R. R. Muñoz et al. (2018b)
ϵ	0.47	⋯	R. R. Muñoz et al. (2018b)
Position angle	73	deg	R. R. Muñoz et al. (2018b)
M_V	-2.56 ± 0.74	mag	R. R. Muñoz et al. (2018b)
L_V	888 ± 605	$L_{V,\odot}$	R. R. Muñoz et al. (2018b)
$v_{\rm sys}$	$-13.0^{+1.1}_{-1.1}$	km s^{-1}	Section 4.1
σ_v	$4.[illegible]^{+1.5}_{[illegible]}$	km s^{-1}	Section [illegible][b]
$M_{1/2}$	$5.9^{+3.7}_{-3.4} \times 10^5$	$M_\odot$	Section 4.1
$({\rm M/L})_{V,1/2}$	[illegible]	$M_\odot/L_{V,\odot}$	Section 4.1
[Fe/H]	$-2.45^{+0.12}_{[illegible]}$	⋯	Section 4.2
$\sigma_{\rm [Fe/H]}$	$0.30^{+0.15}_{-0.11}$	dex	Section 4.2
μ_α^*	0.299 ± 0.052	mas yr^{-1}	Section 6.1
μ_δ	-1.097 ± 0.075	mas yr^{-1}	Section 6.1
$r_{\rm peri}$	$14.7^{+1.0}_{[illegible]}$	kpc	Section 6.1[c]
$r_{\rm apo}$	$43.2^{+0.5}_{-0.5}$	kpc	Section 6.1[c]
e	$0.49^{+0.04}_{-0.05}$	⋯	Section 6.1[c]

Here we list all the properties we measure for Willman I, such as the average velocity of the system, the average chemical abundance of its stars, and its inferred mass!

Notes. List of global structural, kinematic, chemical, and orbital parameters of W1.

[a] The reported distance/distance modulus uncertainty is likely underestimated, as it does not include the systematic contributions from isochrones.

[b] We opt to cite the velocity dispersion determined from our two-component Gaussian mixture model, as it incorporates the uncertainty in membership.

[c] We report the orbital properties determined from `MWPotential2014` of J. Bovy (2015), with the dark matter halo mass scaled up by 50% and the addition of the LMC.

For stars with measured Gaia proper motions and parallaxes, the corresponding membership probabilities for each of these quantities, $P_{\rm pm}$ and $P_{\rm parallax}$, were determined. A. B. Pace et al. (2022) reported proper-motion values of $(\mu^*_{\alpha,\rm W1}, \mu_{\delta,\rm W1}) = (0.255 \pm 0.085, -1.110 \pm 0.096)$ mas yr^{-1} for W1 based on Gaia EDR3 astrometry. For a star with proper motion $(\mu^*_\alpha, \mu_\delta)$ and overall proper-motion uncertainty $\delta_{\rm pm}$ (calculated by summing the two dimensions in quadrature), the membership probability based on proper motion, $P_{\rm pm}$, is defined as (see Figure 1(c)):

$$P_{\rm pm} = \exp\left(-\frac{(\mu^*_\alpha - \mu^*_{\alpha,\rm W1})^2 + (\mu_\delta - \mu_{\delta,\rm W1})^2}{2[(2\sigma_{\rm pm})^2 + \delta^2_{\rm pm}]}\right), \tag{4}$$

where $\sigma_{\rm pm}$ [illegible] A. B. Pace et al. (2022) proper-motion uncertainties added in quadrature. Stars with a proper-motion uncertainty more than twice its signal value are treated as nonmeasurements.

Situated at a distance of ∼39 kpc, the parallax of W1 is immeasurable by Gaia. As we find that the proper-motion membership criterion cleans the sample for the brightest stars, we opt for a simple binary parallax marker: The parallax membership probability is defined as $P_{\rm parallax} = 1$ for stars with parallax-over-error less than 3 and $P_{\rm parallax} = 0$ for stars with parallax-over-error greater than 3.

Finally, $P_{\rm [Fe/H]}$ is determined from the CaT-based metallicity, [Fe/H], for each star. Similar to the other markers, we determine the metallicity membership probability for a star with iron abundance [Fe/H] ± $\delta_{[\mathrm{Fe/H}]}$ as (see Figure 1(d):

$$P_{[\mathrm{Fe/H}]} = \exp\left(-\frac{([\mathrm{Fe/H}] - [\mathrm{Fe/H}]_{\mathrm{W1}})^2}{2[(2\sigma_{[\mathrm{Fe/H}]})^2 + \delta^2_{[\mathrm{Fe/H}]}]}\right), \quad (5)$$

where $[\mathrm{Fe/H}]_{\mathrm{W1}} = -2.1$, the mean spectroscopic metallicity of W1, and $\sigma_{[\mathrm{Fe/H}]} = 0.45$ dex, half the distance between the most metal-poor and metal-rich star in the three star spectroscopic sample of B. Willman et al. (2011). This measurement was chosen as our prior, as it is the largest member sample available with spectroscopic metallicity measurements.

Importantly, our sample identifies seven
nonmembers in the previous 2011 member sample
from our more accurate velocity data and adds
a few new members due to our more sensitive
telescopes.

Beyond these five parameters, there are a few spectral lines covered by DEIMOS that can be incorporated into membership selection to further differentiate between member stars and Milky Way dwarf star contaminants. The NaI absorption line at 8234 Å correlates with surface gravity and can be used to identify Milky Way dwarf stars that display systematically stronger lines than giants (R. P. Schiavon et al. 1997). All stars with $P_{\mathrm{mem}} > 0.5$ have small NaI equivalent widths (< 1 Å within 1σ). Alternatively, G. Battaglia & E. Starkenburg (2012) identified a distinction line between RGB stars and dwarf stars in the equivalent width of the MgI line at 8806.8 Å as a function of the equivalent width of the CaT lines that can also be used to cut Milky Way dwarf star interlopers. Again, all stars with $P_{\mathrm{mem}} > 0.5$ lie within 1σ of the cutoff line, a result that is consistent with the predictions for a metal-poor system. While the use of these NaI and MgI lines is redundant and does not add more layers to our membership selection, they are a useful tool for validating that our selection criterion are efficiently differentiating between W1 members and Milky Way foreground stars.

Now we can use our member sample to measure
structural and kinematic properties of Willman I.
This, in turn, will help us answer our two science
questions:

(1) Is Willman I a dwarf galaxy or a star cluster?
(2) Is Willman I in dynamical equilibrium?

3.2. Final Member Sample and Comparison to Literature Samples

The membership probability, P_{mem}, of each star is shown in the bottom panels of Figure 1. From this, we define stars with $P_{\mathrm{mem}} > 0.5$ as members of W1. This results in 56 members, all but one of which lie within 3 $r_{\mathrm{half,ell}}$. We recognize the subjectiveness of this probability cutoff and take this into account when calculating the properties of W1 (see Section 4.1). Multiple velocity epochs exist for 36 of the 56 stars in our sample, from which we identify six velocity variables, including one blue straggler. We infer the physical parameters of W1 from the 49 members within 3 $r_{\mathrm{half,ell}}$, and these properties are presented in Table 2.

As shown in Figure 2, we report that 28 members are inside the elliptical half-light radius, 19 of which have multiple velocity epochs and nonvariable velocities. We highlight that, despite implementing no spatial cuts, the stellar density distribution of our member sample shows no stars in excess of a Plummer profile. The CMD of W1 members is consistent with that of an old, metal-poor system, and we identify eight RGB stars for which we measure spectroscopic metallicities.

All 45 published members in B. Willman et al. (2011) overlap with the Keck/DEIMOS spectroscopy within 1.″5. Due to more stringent quality criteria, seven stars in the 2011 sample lack velocity measurements in this work due to low S/N and poor velocity fits; they are thus not considered for membership. A total of 31 stars in the 2011 sample overlap with the 56 member stars in this work. The seven remaining stars in the 2011 sample are labeled as nonmembers: four on the basis of proper-motion/parallax estimates from Gaia and three due to updated velocities that are inconsistent with the systemic motion of W1. We also find the presence of four stars flagged as binaries by this work in the 2011 sample. Of the 52 foreground Milky Way stars reported in B. Willman et al. (2011), 51 stars have matches with our measured velocities. One of these stars is included in our member sample based on an updated velocity measurement, and we confirm the remaining stars as nonmembers.

The completeness of our kinematic sample was evaluated by comparing with the CFHT MegaCam photometric catalog from R. R. Muñoz et al. (2018a). This photometric catalog was restricted to stars within 3 $r_{\mathrm{half,ell}}$ and $P_{\mathrm{CMD}} \geqslant 0.5$, ensuring that we only evaluate the completeness of our sample against likely member stars (see Figure 2). All stars with $r_0 \leqslant 21$ inside 1 half-light radius have spectroscopic measurements and are included in our analysis. For fainter stars ($r_0 \leqslant 23$), the spectroscopic completeness decreases approximately linearly from 100% to 70% from 0 to 3 $r_{\mathrm{half,ell}}$.

4. Results

With a sample of 49 W1 members within 3 $r_{\mathrm{half,ell}}$ with measured velocities, we next probe the kinematic (Section 4.1) and chemical (Section 4.2) properties of this system.

4.1. Velocity Dispersion and Dynamical Mass

Based on our member sample, we present the velocity profile of W1 in Figure 3. B. Willman et al. (2011) reported a peculiar velocity profile where stars within ∼0.75 $r_{\mathrm{half,ell}}$ are offset from those in the outskirts, which they note as difficult to explain with an equilibrium model. This phenomenon is still observed by visual inspection in our updated member sample (see Figure 3, top panel). Quantitatively, the rolling average decreases by about 8.5 ± 3.0 km s^{-1} from the center to the outskirts of W1. We find that this gradient is not obviously explained by ordered rotation (see Figure 3, bottom panel).

We calculate the systemic velocity and velocity dispersion of W1 using a two-component Gaussian mixture model to simultaneously model the Milky Way and W1. We opt for this approach, as it separates the two populations without imposing a strict membership threshold, allowing the inferred velocity dispersion to marginalize over contamination from Milky Way foreground stars (e.g., G. D. Martinez et al. 2011).

We begin by eliminating obvious nonmembers from our full dataset using the membership probabilities determined in Section 3.1. We define obvious nonmembers as stars whose membership probability without velocity ($P_{\mathrm{mem,nov}} \propto P_{\mathrm{CMD}} \times P_{\mathrm{pm}} \times P_{\mathrm{parallax}} \times P_{[\mathrm{Fe/H}]}$) is <0.1 or stars with large radial velocities ($|v| > 150\,\mathrm{km\,s^{-1}}$). This results in 65 stars within 3 $r_{\mathrm{half,ell}}$. Our results are not sensitive to our membership or velocity cutoff choices within the reported uncertainties. We then apply a two-component Gaussian maximum likelihood function, whose total log likelihood takes the form (M. G. Walker et al. 2006):

$$\ln \mathcal{L} = \sum_i \ln [f \cdot \mathcal{N}(v_i \mid v_{\mathrm{W1}}, \sigma^2_{\mathrm{W1}} + \delta v_i^2) + (1 - f) \cdot \mathcal{N}(v_i \mid v_{\mathrm{MW}}, \sigma^2_{\mathrm{MW}} + \delta v_i^2)],$$

where f is the fraction of W1 members in our dataset, v_{W1} is the systemic velocity of W1, σ_{W1} is the velocity dispersion of W1, v_{MW} is the systemic velocity of the Milky Way, and σ_{MW}

Velocity:

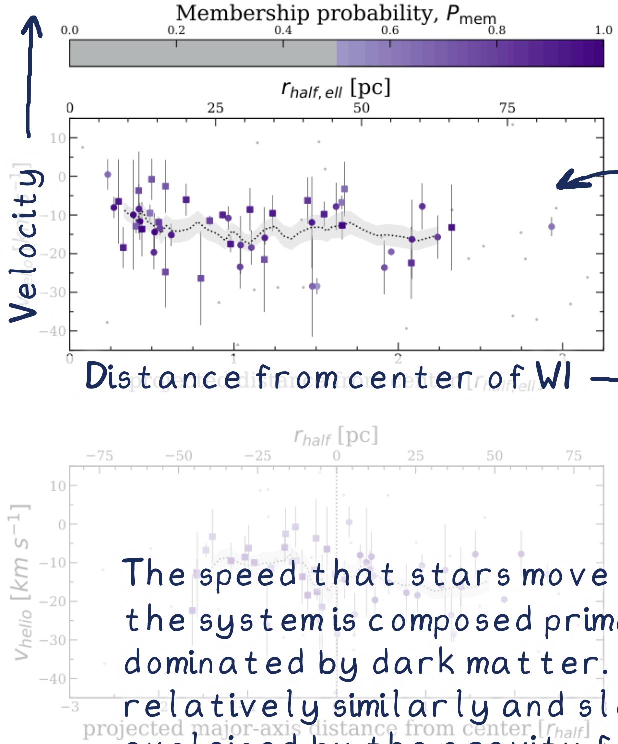

We observe that Willman I has a weird velocity profile. Stars near the center of Willman I have higher velocities than stars near the outskirts.

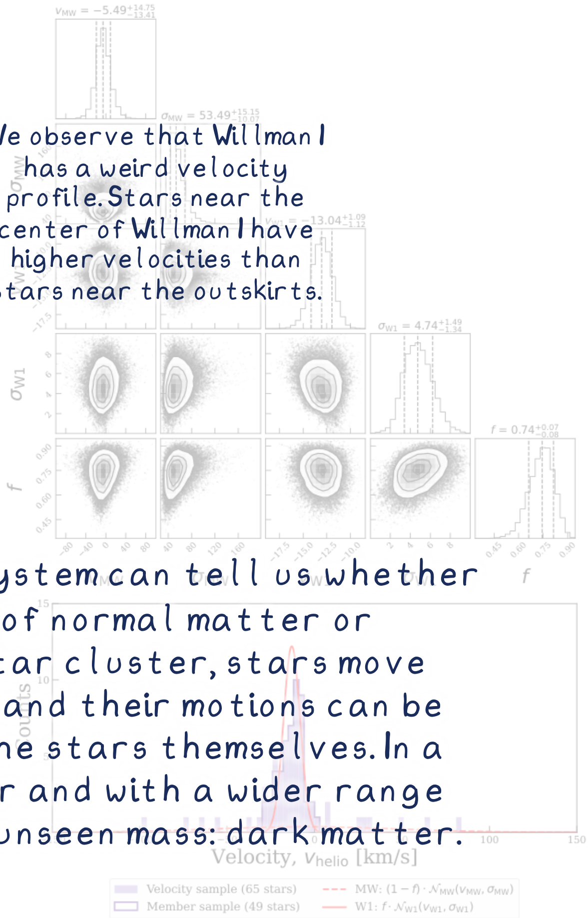

The speed that stars move in a system can tell us whether the system is composed primarily of normal matter or dominated by dark matter. In a star cluster, stars move relatively similarly and slowly, and their motions can be explained by the gravity from the stars themselves. In a dwarf galaxy, stars move faster and with a wider range of speeds because of additional unseen mass: dark matter.

Astronomers measure this using a quantity called the velocity dispersion, a description of how spread out the velocity distribution of stars is. We find the velocity dispersion of Willman I to be non-zero, suggesting the presence of dark matter.

From the velocity dispersion, we can also infer the dynamical mass of the system assuming equilibrium. The dynamical mass refers to how much mass is in the system based on the motions of stars, not just by counting the mass of stars. If the dynamical mass is much larger than what is expected from the starlight, this suggests the presence of dark matter. This is what we find to be the case for Willman I.

Figure 3. Heliocentric radial velocities and uncertainties of the 49 members as a function of elli[illegible] (top panel) and [illegible] with respect to the major axis (bottom panel). For both plots, stars to the left and the right of the cent[illegible] respectively. All 49 stars are color-coded purple according to their membership probability, and nonmembers are in gray. In both panels, the dotted black line represents the membership probability weighted seven-star rolling velocity average, and the gray shaded region represents the uncertainty in the rolling average calculated via bootstrapping.

is the velocity dispersion of the Milky Way. We account for the velocity measurement uncertainty of each star, δv_i, by adding it in quadrature to the intrinsic dispersion of each Gaussian.

To sample this model, the MCMC sampler emcee (D. Foreman-Mackey et al. 2013) was run using 20 walkers. We initialize [illegible] with the values from B. Willman et al. (2011) for W1 ($v_{W1} = -12.8$ km s^{-1}, $\sigma_{W1} = 4.8$ km s^{-1}), reasonable values for the Milky Way ($v_{MW} = 0$ km s^{-1}, $\sigma_{W1} = 50$ km s^{-1}), and a member fraction equivalent to the fraction of our determined member sample ($f = 0.75$), but our results are not dependent on these choices. We adopt the following uniform priors for our five parameters: $-100 < v_{MW} < 100$ km s^{-1}, $0 < \sigma_{MW} < 200$ km s^{-1}, $-30 < v_{W1} < 10$ km s^{-1}, $0 < \sigma_{W1} < 10$ km s^{-1}, and $0 < f < 1$. The distribution of posterior samples is shown in the top panel of Figure 4. We measure the systemic velocity as the sample median and the associated uncertainties from 16th and 84th percentiles.

The systemic velocity of W1 is estimated to be $v_{sys} = -13.0^{+1.1}_{-1.1}$ km s^{-1} with a velocity dispersion of $\sigma_v = 4.7^{+1.5}_{-1.3}$ km s^{-1}, which is consistent with measurements by B. Willman et al. (2011) and M. Geha et al. (2026). We highlight that the velocity dispersion is degenerate with the member fraction, implying that the large uncertainty in W1's velocity dispersion is driven by the uncertainty in identifying a

Figure 4. Top panel: Posterior samples for the two-component Gaussian mixture model to measure the systemic velocity and velocity dispersion of W1 based on a velocity sample of 65 potential member stars within 3 $r_{half,ell}$. The [illegible] and 84th percentiles. Bottom panel: Best-fit mixture model of two-component Gaussian representing the Milky Way and W1. The 65 potential members used for our fitting are overplotted, and the member sample (Section 3.2) is outlined in purple. We [illegible] comment on this in Section 7.2.

pure member sample. This result is unchanged within the reported uncertainty when restricting the sample to anywhere within 2 to 4 $r_{half,ell}$, or when restricting the sample to only stars with multiple velocity epochs. When cutting the sample to 1 $r_{half,ell}$, the uncertainty on the velocity dispersion grows such that the system is not conclusively resolved due to the small sample size of stars. Notably, the kinematic distribution of W1 [illegible] that a single global velocity dispersion value is insufficient to fully characterize the complex kinematic profile of W1 (see Figure 4, bottom panel). [illegible] dynamical mass of W1 within its half-light radius can be inferred from this radial velocity dispersion. Following the methods of J. Wolf et al. [illegible] radius is estimated to be [illegible] a central mass-to-light ratio of $(M/L)_V = 660 \pm 590$. This is consistent with the dynamical mass and mass-to-light ratio previously determined by B. Willman et al. (2011) ($\sim 3.9^{+2.5}_{-1.6} \times 10^5\ M_\odot$; $(M/L)_V = 770^{+930}_{-440}$; note that we use an updated M_V value causing the mass-to-light ratio in this work to be smaller despite a larger mass).

Metallicity:

The metallicity of stars, or the amount of heavy (not hydrogen or helium) elements present, tells us how a system formed and evolved. Star clusters typically form their stars in a single burst, so all their stars have very similar metallicities. On the other hand, dwarf galaxies form stars over longer periods of time, leading to a wider range of metallicities.

For Willman I, we are able to measure metallicities for eight bright stars in our sample. We find that there is a wide spread in metallicity between these stars indicating multiple generations of star formation, consistent with what we would expect from a dwarf galaxy.

The member fraction estimated from our mixture model [illegible] $= 0.74^{+0.07}_{-0.08}$, which is consistent with the number of members determined in Section 3. We find similar results when employing a single Gaussian maximum likelihood model on our member sample of 49 stars within $3\,r_{\rm half,ell}$. From this method, the systemic velocity of W1 is measured to be $v_{\rm sys} = -12.8^{+1.0}_{-1.0}$ km s^{-1} with a velocity dispersion of $\sigma_v = 4.8^{+0.9}_{-0.8}$ km s^{-1}. Requiring multiple velocity epochs or reducing the half-light radius cutoff down to $2\,r_{\rm half,ell}$ does not alter the systemic velocity or velocity dispersion beyond the uncertainties determined. These results are consistent with the two-component Gaussian, [illegible] with likely underestimated uncertainties. As such, we emphasize our values from the mixture model, which incorporate the uncertainty in membership as well. Table A1 presents the measured properties of all 72 stars considered in our analysis, including the 65 stars used in the mixture model and the 56 stars in the final member sample.

4.2. Metallicity Distribution

As detailed in Section 2.2, we are able to infer [Fe/H] measurements for the stars in our member sample based on CaT equivalent width measurements. This calibration is only valid for RGB stars ($M_V < 3$), significantly reducing our member sample to eight stars with measured metallicities, all of which are within $2\,r_{\rm half,ell}$ (see Figure 2, bottom panel; Figure 5, top panel). From this sample, we determine the CaT-based mean metallicity and metallicity dispersion using an MCMC sampler with 20 walkers to sample from a Gaussian maximum likelihood function (D. Foreman-Mackey et al. 2013; M. G. Walker et al. 2006). We opt not to use a mixture model as performed in Section 4.1 due to the small sample size (see Figure 1(h)). We initialize our walkers using the values determined by B. Willman et al. (2011) ([Fe/H] $= -2.1$, $\sigma_{\rm [Fe/H]} = 0.45$ dex). The median and 16th and 84th percentiles of the resulting posterior distribution function are presented.

The metallicity of W1 is measured to be [Fe/H] $= -2.45^{+0.12}_{-0.13}$ with a metallicity dispersion of $\sigma_{\rm [Fe/H]} = 0.30^{+0.15}_{-0.11}$ dex (see Figure 5). The removal of the highest-metallicity star slightly lowers the measured average metallicity and substantially reduces the measured metallicity spread (to [Fe/H] $= -2.53^{+0.08}_{-0.09}$, $\sigma_{\rm [Fe/H]} = 0.12^{+0.12}_{-0.08}$ dex). We emphasize that this star has a high membership probability ($P_{\rm mem} \sim 0.9$) and that the mean metallicity without this star is still within the uncertainties derived with the full sample.

B. Willman et al. (2011) measured a metallicity spread in W1 based on Keck/DEIMOS spectroscopy of three RGB members ([Fe/H] $= -1.73 \pm 0.12$, -2.65 ± 0.12, and -1.92 ± 0.21). These three stars are in our member sample, although we report slightly lower-metallicity values for two of these stars ([Fe/H] $= -2.32 \pm 0.13$, -2.56 ± 0.13, and -2.61 ± 0.19, respectively). In comparison with the photometric metallicity values derived from HST CaHK imaging from S. W. Fu et al. (2023) ([Fe/H] $= -2.53^{+0.11}_{-0.11}$, $\sigma_{\rm [Fe/H]} = 0.65^{+0.10}_{-0.09}$ dex), we measure W1 to be a slightly more metal-rich system with a substantially smaller metallicity dispersion.

5. Mass Segregation

We now shift our attention to the HST/ACS data (Section 5.1), evaluating the presence of stellar mass segregation, which can be used to differentiate between a galactic and star cluster origin for W1 (Section 5.2).

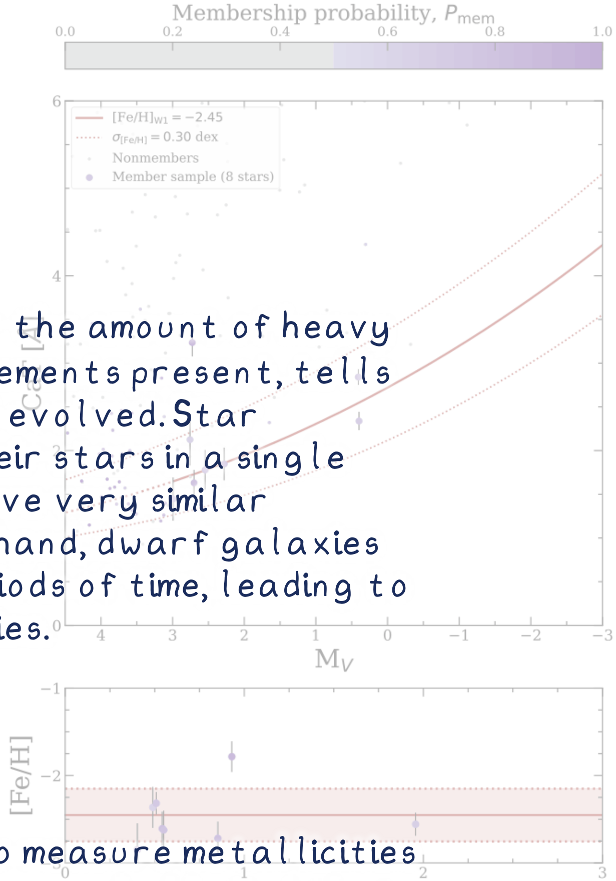

Figure 5. CaT equivalent width as a function of V-band magnitude (top panel) and the CaT-based spatial metallicity distribution (bottom panel) for the eight RGB stars in our member sample. The solid line denotes the calibration range of the empirical relationship of R. Carrera et al. (2013) plotted at the mean metallicity of W1 while the dotted lines represents the metallicity dispersion determined from MCMC sampling.

5.1. HST/ACS Imaging

W1 was observed by HST in 2017 as part of the Treasury Program GO-14734 (PI: Kallivayalil). Deep photometry of W1 was obtained with ACS (H. C. Ford et al. 1998) using the Wide Field Channel (WFC). The ACS/WFC field approximately covers the inner half-light radius of W1 (see Figure 2, top panel). Observations were split evenly between the F606W and F814W filters with a combined exposure time of 9254 s.

For the analysis below, we use the same HST data reduction as described in H. Richstein et al. (2024). Briefly, the individual exposures from each filter were aligned and coadded using DrizzlePac, an HST software package. The combined output images were then masked with the `segmentation` routine from the `photutils` package (L. Bradley et al. 2025). Point-spread function (PSF)-fitting photometry was performed on the combined images using DAOPHOT-II and ALLSTAR (P. B. Stetson 1987, 1992). The source lists from F606W and F814W were matched using DAOMATCH and DAOMASTER to create a preliminary PSF source catalog. An empirically derived aperture correction was

Mass segregation:

The presence of mass segregation can be used as a diagnostic to determine if a system is a star cluster or a dwarf galaxy. Mass segregation is the process by which high-mass stars sink towards the center of the system while low-mass stars drift to the outskirts. This feature is present in globular clusters, but not in dwarf galaxies. The massive amounts of dark matter in dwarf galaxies extend the timescale for this process beyond the age of the Universe!

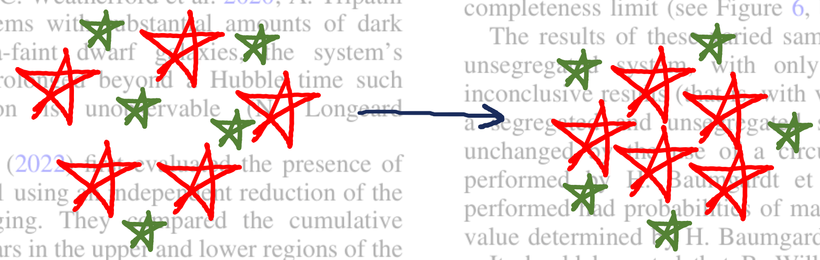

To test for mass segregation in Willman I, we separate stars into high-mass stars and low-mass stars based on how bright they are. Then, we look at whether there are systematically more high mass stars near the center compared to the low mass stars. This is using about 600 stars identified in images of Willman I taken with the *Hubble Space Telescope*.

---

applied to the magnitudes, which were then converted to the Vega Mag system and adjusted for the exposure time. Finally, to address star–galaxy separation, each source was assigned a quality flag from 0 to 1 based on how closely its parameters matched those in artificial star tests across different filters.

We also note that M. J. Durbin et al. (2025) used HST imaging to measure the star formation histories of 56 ultrafaint dwarf galaxies, including W1. Their results indicate that 50% of W1's stellar mass formed $\tau_{50} = 13.44^{+0.00}_{-0.81}$ Gyr and 90% of W1's stellar mass formed before $\tau_{90} = 8.37^{+[illegible]}_{-0.93}$ Gyr, indicating a uniformly ancient stellar population formed from an early burst of star formation. We obtain consistent results when performing a similar star formation history analysis on this dataset.

5.2. Mass Segregation Determination

The presence of mass segregation can be used as a diagnostic for determining whether a system is a star cluster or a dwarf galaxy (H. Baumgardt et al. 2022). Due to the equipartition of kinetic energy whereby high-mass stars transfer energy to low-mass stars over time, high-mass stars tend to aggregate near the center of systems while low-mass stars drift toward the outer regions. This process occurs over the course of a few relaxation periods, and is thus a significant feature in old stellar objects with relatively short relaxation periods compared to their age, such as globular clusters (e.g., D. Kim et al. 2015; N. C. Weatherford et al. 2020; A. Tripathi et al. 2023). For systems with substantial amounts of dark matter, such as ultra-faint dwarf galaxies, the system's relaxation period is prolonged beyond a Hubble time such that mass segregation is unobservable (N. Longeard et al. 2018).

H. Baumgardt et al. (2022) first evaluated the presence of mass segregation in W1 using an independent reduction of the same HST/ACS imaging. They compared the cumulative radial distribution of stars in the upper and lower regions of the main sequence, constructing two samples: one of bright, higher-mass stars and the other of faint, lower-mass stars. In highly segregated systems, such as globular clusters, the ratio of half-light radii for these two samples usually lies around 0.7. For W1, H. Baumgardt et al. (2022) measured a ratio of $R_{\mathrm{half,bright}}/R_{\mathrm{half,faint}} = 1.05 \pm 0.08$, indicating a lack of mass segregation and evidence toward a dwarf galaxy classification.

Loosely following the methods of H. Baumgardt et al. (2022), we reanalyze the same HST/ACS data to independently evaluate the possibility of mass segregation in W1. We begin by removing extragalactic sources, defined as those with star quality flags <0.5. To isolate the probable members in W1, we compared the CMD of the 1055 remaining stars to an old, metal-poor isochrone from the `MIST` stellar evolutionary track models ([illegible] 12 Gyr, [Fe/H] = −2.2), shifted to a distance modulus of $m - M = 17.93$, which corresponds to a distance of 38.55 kpc), accounting for interstellar reddening (D. J. Schlegel et al. 1998; M. Sirianni et al. 2005; J. Choi et al. 2016; A. Dotter 2016). We define members as stars with the greater of either 0.15 mag or twice their photometric uncertainty from the isochrone. Finally, due to the limited field of view of the ACS/WFC compared to the extended spatial distribution of W1, only stars contained within 1 $r_{\mathrm{half,ell}}$ were included to ensure that the mass segregation profile was not controlled by just a few outlying stars. Our final sample consists of 635 stars.

We first use the MS turnoff and the estimated location of 0.5 $M_\odot$ stars included in the synthetic isochrone as upper and lower photometric bounds. The stars that passed the spatial and CMD cuts within these bounds were divided into two groups of equal size based on stellar brightness to create two separate samples of bright and faint stars (see Figure 6, top-left panel). The radial cumulative distribution of stars for each sample was determined using an elliptical aperture with half-light radius, position angle, and ellipticity values from N. F. Martin et al. (2008; see Table 2). The half-light radius for each sample was defined as the elliptical radius within which half of the stars of each sample are contained.

H. Baumgardt et al. (2022) estimated that the expected half-light ratio between bright and faint stars for a star cluster the size of W1 is 0.90, a value that would only be more extreme if W1 is tidally disturbed as both mass segregation and tidal stripping would preferentially remove most stars from the central regions (N. E. Q. Paust et al. 2009). We obtained a half-light radius ratio of $R_{\mathrm{half,bright}}/R_{\mathrm{half,faint}} = 1.05 \pm 0.08$, where the uncertainty is calculated by bootstrapping over each sample (see Figure 6, top-right panel). A standard two-sample Kolmogorov–Smirnov (K-S) test shows a <1% probability of mass segregation, which we highlight as a more comprehensive test statistic that takes into account the full distributions rather than evaluating the discrepancy between distributions at a single location. This process was repeated using varying lower-bound cutoffs all the way down to the 50% photometric completeness limit (see Figure 6, bottom panels).

The results of these varied samples are consistent with an unsegregated system, with only a few samples showing inconclusive results (that is, with values compatible with both a segregated and unsegregated system). These results are unchanged by the use of a circular aperture, as originally performed by H. Baumgardt et al. (2022). All K-S tests performed had probabilities of mass segregation <29.7%, the value determined by H. Baumgardt et al. (2022).

It should be noted that B. Willman et al. (2006) presented evidence for mass segregation using ground-based photometry to compare the luminosity function (LF) of stars in the central and tail regions. Observing an excess of low-luminosity stars in the tail region, they performed a K-S test that showed a 68% chance that the two stellar LFs were drawn from different populations, which was interpreted as evidence for mass segregation. To revisit this claim using a larger sample size and deeper photometry, the 635 HST member stars were divided into two samples by implementing similar cuts to (B. Willman et al. 2006, see their Figure 4): central stars within 0.5 $r_{\mathrm{half,ell}}$ and outer stars beyond 0.5 $r_{\mathrm{half,ell}}$. As carried out by B. Willman et al. (2006), the LF for each sample was determined, and an offset value was added to the central region sample to correct for a difference in sample size and facilitate direct comparison. No surplus of low-luminosity stars is observed in the outer stars, and performing a two-sample K-S test on the inner and outer sample LFs shows a <10% probability that the two LFs were drawn from different populations, which we interpret as additional evidence that W1 is unsegregated. As one final check, this process was repeated for 56 member stars from our analysis of the DEIMOS data (Section 3.2), which also show no excess of low-luminosity stars at the outskirts. Thus, we find no evidence for mass segregation in W1, consistent with the results of H. Baumgardt et al. (2022). This supports a dwarf galaxy classification for the system.

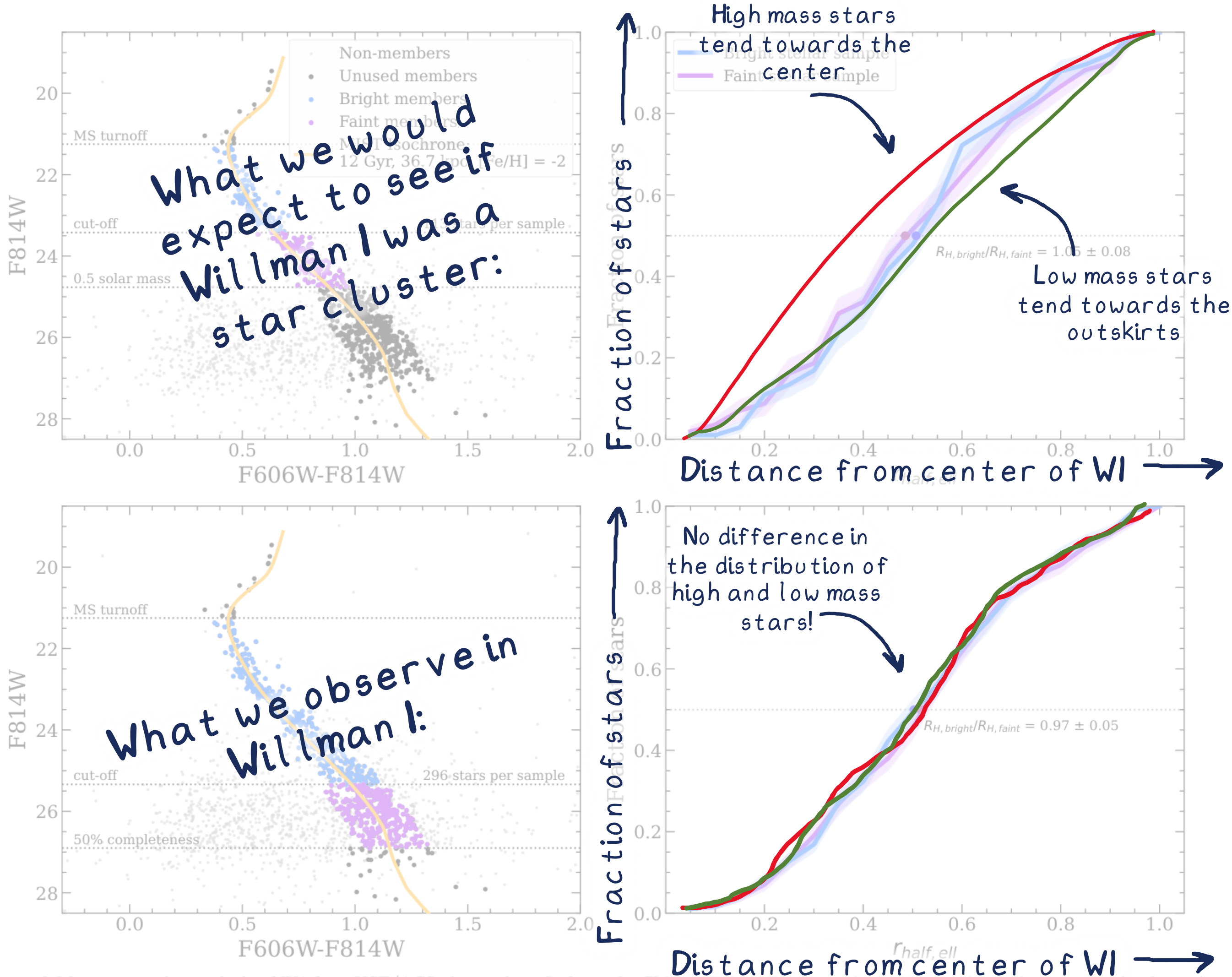

What we would expect to see if Willman I was a star cluster:

High mass stars tend towards the center

Low mass stars tend towards the outskirts

Fraction of stars

Distance from center of WI

What we observe in Willman I:

No difference in the distribution of high and low mass stars!

Fraction of stars

Distance from center of WI

Figure 6. Mass segregation analysis of W1 from HST/ACS observations. Left panels: CMD of W1 HST data overlaid with an old, metal-poor `MIST` isochrone in orange. Blue and purple stars show the stars selected based on different magnitude cuts (top panels = 0.5 $M_{\odot}$; bottom panels = 50% completeness threshold) to calculate the mass segregation profile. Right panels: Corresponding average cumulative elliptical radial distribution of stars. The shaded region corresponds to the 1σ uncertainty calculated by bootstrapping over each sample. No significant signs of mass segregation are detected.

We thus find no evidence for mass segregation in Willman I!

6. Dynamical History

We next investigate the possibility of past tidal interaction between the Milky Way and W1 by examining the orbital history of W1 (Section 6.1) and simulating mock stellar streams (Section 6.2).

6.1. Orbit

We compute the orbit of W1 using the analytic potential `MWPotential2014` of the `galpy` package by J. Bovy (2015). This model of the Milky Way's gravitational potential consists of a power-law spherical potential representing the bulge (J. Binney & S. Tremaine 1987), a Miyamoto–Nagai disk potential (M. Miyamoto & R. Nagai 1975), and a Navarro–Frenk–White dark matter halo potential (J. F. Navarro et al. 1997). From this, we integrate the orbit of W1 backwards in time based on its six-dimensional phase-space coordinates (see Table 2 for values). We measure a proper motion of $(\mu_{\alpha}^{*}, \mu_{\delta}) = (0.299 \pm 0.052, -1.097 \pm 0.075)$ mas yr^{-1} by using a single Gaussian maximum likelihood model on the seven stars in our member sample with measured Gaia proper motions (see Figure 1(g)). This is consistent with the results of A. B. Pace et al. (20[illegible]), who applied background mixture models to Gaia EDR3 data, both in measurement value and the number of Gaia members.

Previous orbital analyses of Milky Way dwarf galaxies have reported moderately small pericenter distance values for W1 (ranging from 16–44 kpc; J. D. Simon 2018; B. M. Armstrong et al. 2021; A. B. Pace et al. 2022), but are highly dependent on membership selection and the assumed Milky Way potential. To probe the effect of different assumed Milky Way potentials, we also model W1's orbit using two other potentials. The estimated mass of the Milky Way's dark matter halo for `MWPotential2014` is on the lower end with a value of $0.8 \times 10^{12} M_{\odot}$. To account for this uncertainty, the second potential we adopt is the same `MWPotential2014` with a 50% larger dark matter halo mass ($1.2 \times 10^{12} M_{\odot}$). The Large Magellanic Cloud (LMC) has also been known to affect the orbits of objects, even those distant from it, due to the reflex motion of the Milky Way's orbit

Orbital modeling:

The orbit of a system tells us how it has moved through the Milky Way. If close enough, it may have been affected by the Galaxy's gravity that can stretch and disrupt the system.

Given the current position and velocity of Willman I, we can use a model of the Milky Way to simulate the orbit of Willman I backwards in time. We find that Willman I is currently at the furthest point in its orbit after passing near the Galactic center, when and where it might have been affected by the Galaxy's gravitational influence.

(e.g., D. Erkal et al. 2021; A. P. Ji et al. 2021; L. Correa Magnus & E. Vasiliev 2022; E. Patel et al. 2024). This MW +LMC potential is the third and final potential we use to calculate the orbit of W1, where the LMC is modeled by a moving Hernquist potential of mass $1.38 \times 10^{11}\,M_\odot$ and scale radius of 8.7 kpc, taking into account dynamical friction (L. Hernquist 1990; R. P. van der Marel & N. Kallivayalil 2014; J. Bovy 2015). We find the dynamical friction of W1 to have a negligible impact on its orbit. Due to uncertainty in orbit integration models beyond one orbital period (especially for satellites with pericenter distances <30 kpc; R. D'Souza & E. F. Bell 2022; R. F. G. Machado et al. 2025), we use these potentials to model the three-dimensional orbit of W1 over only the last 1 Gyr with a time resolution of 1 Myr.

Figure 7 compares the modeled orbits of W1 using these three different Milky Way potentials. The orbital period predicted by the original MWPotential2014 is larger than the other two potentials by ∼0.2 Gyr. In all cases, W1 is at apocenter, coming from a position closer to the Galactic center, although the exact pericenter distance of the orbit depends on the potential used.

Due to the uncertainties in distance, velocity, and proper motion measurements, the uncertainty in the orbit of W1 was calculated through Monte Carlo sampling. We create 1000 six-dimensional phase-space coordinates by sampling distance, velocity, and proper-motion values from Gaussian distributions based on each parameter's average estimated value and 1σ standard deviation (see Table 2). The reported distance uncertainty from M. J. Durbin et al. (2025) is likely underestimated, as it does not include systematic contributions from the isochrones. Our orbital solutions remain conclusively consistent with a system moving away from a position closer in to the Milky Way up to distance uncertainties of ∼3 kpc.

This procedure was performed for both the regular `MWPotential2014` and the potential with the addition of the LMC (see Figure 7). The orbit of W1 under the regular `MWPotential2014` has a pericenter distance of $r_{\rm peri} = 24.9^{+3.5}_{-3.1}$ kpc, an apocenter distance of $r_{\rm apo} = 43.5^{+0.4}_{-0.5}$ kpc, and an eccentricity $e = 0.27^{+0.06}_{-0.06}$. The addition of the LMC modifies these predictions, simulating a pericenter distance of $r_{\rm peri} = 14.7^{+1.9}_{-1.6}$ kpc, an apocenter distance of $r_{\rm apo} = 43.2^{+0.5}_{-0.5}$ kpc, and an eccentricity of $e = 0.49^{+0.04}_{-0.05}$. These reported parameters represent the median of our sampling procedure, and the uncertainties represent the 16th and 84th percentiles. None of the orbital samples for both potentials have pericenter distances >40 kpc, indicating that the trajectory of W1 is most likely to be coming out of the Milky Way approaching apocenter.

To quantitatively verify that W1 is at apocenter, we calculate the ratio $f_{\rm peri}$ of T. K. Fritz et al. (2018):

$$f_{\rm peri} = \frac{r - r_{\rm peri}}{r_{\rm apo} - r_{\rm peri}}, \quad (6)$$

which is a proxy for the orbital phase in the radial direction. $f_{\rm peri} = 0$ and 1 indicate an object at pericenter and apocenter, respectively. For both the regular `MWPotential2014` and with the addition of the LMC, the ratio was determined to be $f_{\rm peri} = 0.99 \pm 0.01$, consistent with our conclusion that W1 is being observed at or very near apocenter after spending time closer to the Galactic center.

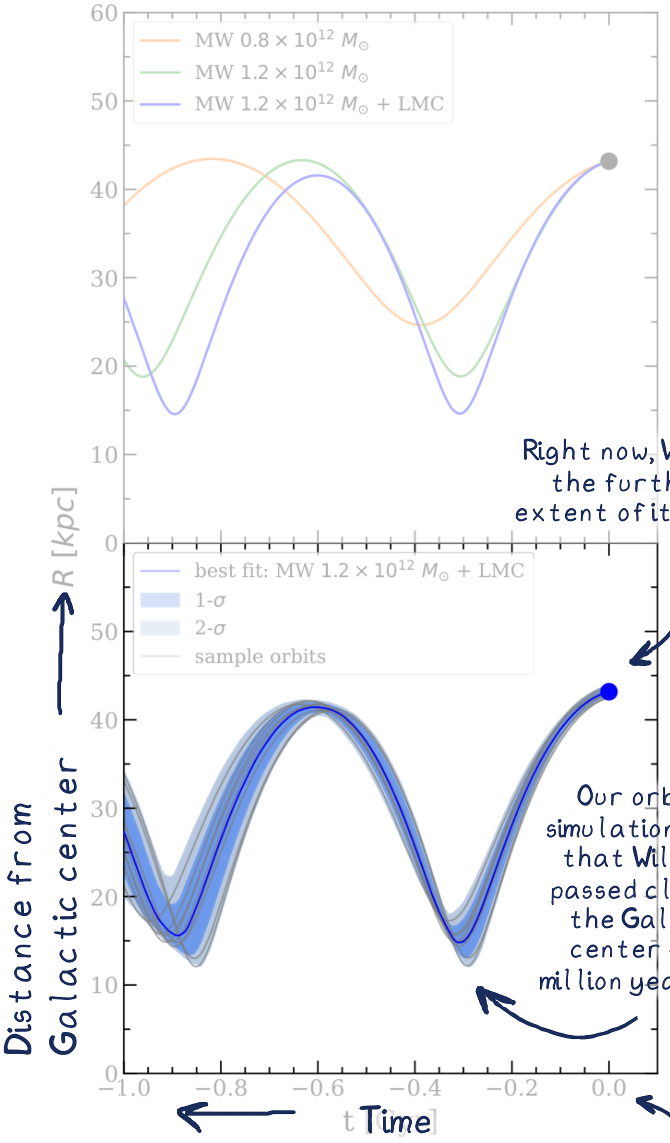

Right now, WI is at the furthest extent of its orbit

Our orbital simulations show that Willman I passed close to the Galactic center ~300 million years ago!

Present day is here! And we are looking backwards in time

Figure 7. Orbit of W1. Top panel: Distance of W1 to the galactic center as a function of time using three different Milky Way potentials from J. Bovy (2015) orbital simulations. Bottom panel: The same as above but only showing the orbital simulations using `MWPotential2014` of J. Bovy (2015), with the dark matter halo mass scaled up by 50% and the addition of the LMC. The blue line represents the 50th percentile orbit from Monte Carlo sampling over our six-dimensional phase-space parameter uncertainties; the dark-blue shaded region represents the space within the 16th and 84th percentile orbits; and the light-blue region represents the space between the 5th and 95th percentile orbits.

From the estimate of the central dynamical mass of W1 ($M_{\rm W1}$), the Jacobi tidal radius of W1 (R_J) as a function of orbital radius ($R_{\rm W1}$) can be approximated (K. A. Innanen et al. 1983):

$$R_J(R_{\rm W1}) = \left(\frac{M_{\rm W1}}{3M_{\rm MW}}\right)^{1/3} R_{\rm W1}. \quad (7)$$

The mass of the Milky Way enclosed within the orbital radius of the satellite ($M_{\rm MW}$) was determined from `MWPotential2014` with a dark matter halo mass enlarged by 50% ($1.2 \times 10^{12}\ M_\odot$). From this, the current Jacobi tidal radius of W1 is estimated to be $R_J = 220^{+120}_{-140}$ pc, which

Now, let's apply all that we have learned about Willman I to answer our two main science questions!

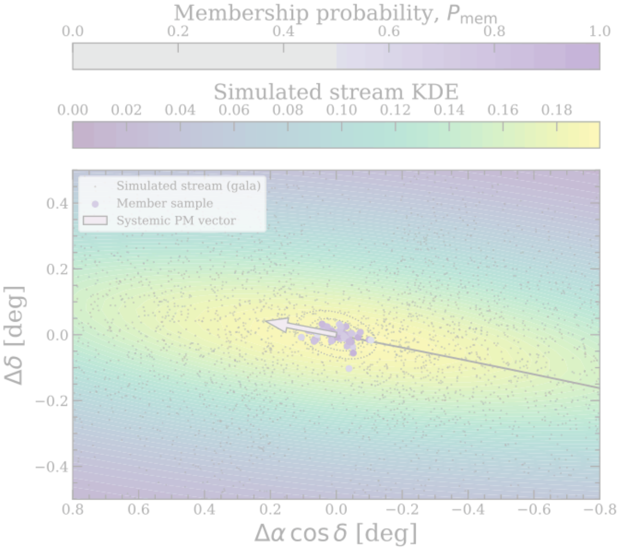

Figure 8. Spatial distribution of simulated particles from `gala` mock stream spray model using `MWPotential2014` of J. Bovy (2015) with a 50% enlarged dark matter halo ($1.2 \times 10^{12}\,M_\odot$). The member sample is overplotted and color-coded according to their membership probability. The systemic proper-motion vector corrected for solar-reflex motion is denoted by the light-purple arrow, and the three concentric dotted ellipses represent 1, 2, and 3 $r_{\rm half,ell}$.

corresponds to $7.7^{+1.6}_{-1.8}$ half-light radii. In comparison, the tidal radius of W1 at pericent[illegible] pc, which is equivalent to $3.1^{+0.8}_{-0.8}$ half-light radii. These orbit integrations suggest that, at pericenter, th[illegible] a few half-light radii of its center.

The current dynamical prop[illegible] correspond to their infall time, as shown by M. Rocha et al. (2012) using subhalos from the Via Lactea II cosmological simulations. Their work found a tight correlation between orbital energy and infall time where subhalos that were accreted earlier had more time to sink into the gravitational potential of the Milky Way, resulting in energies corresponding to more tightly bound systems (M. Rocha et al. 2012, see their Figure 2). Tightly bound objects cluster at small Galactocentric radii and low speeds (M. Rocha et al. 2012, see their Figure 3), consistent with the properties of W1 (see Section 7.2). Indeed, our orbital model for W1 suggests that W1 is one of the most tightly bound dwarf galaxies based on its total energy. From this relation, we estimate W1's infall time to be roughly 9 Gyr ago. Combining this with an orbital period of ∼0.6 Gyr (see Figure 7, bottom panel), we can estimate that W1 has undergone ∼15 orbits since it crossed into the virial radius of the Milky Way.

6.2. Mock Tidal Streams

To further probe the possibility of tidal interactions between the Milky Way and W1, we use the `gala` particle stream spray to generate simulated stellar streams for comparison with the distribution of W1 stars (A. M. Price-Whelan 2017). We adopt the same six-dimensional phase-space coordinates and Milky Way gravitational potential as used in the orbit integration (`MWPotential2014`, 50% enlarged dark matter halo of J. Bovy 2015). The mass of the simulated progenitor was set to $5.9 \times 10^5\,M_\odot$ (the central dynamical mass of W1 determined in Section 4.1), and a scale radius of 26.8 pc (the half-light radius of W1) was used to represent W1. The self-gravity of W1 was modeled by a Plummer potential (H. C. Plummer 1911; B. Willman et al. 2011). The orbit of W1 was integrated backward in time over 1 Gyr in 1 Myr intervals, and then re-integrated forward in time to the present spraying particles at each of the two Lagrange points at each time step following the Fardal Stream distribution function (M. A. Fardal et al. 2015).

Figure 8 presents the results of these simulations. The mock streams exhibit a large spatial spread, with the highest-density regions approximately along W1's semimajor axis. This orientation is also aligned with W1's orbital trajectory and average solar-reflex-corrected proper-motion vector, consistent with expectations for tidal stripping along the orbit.

7. Discussion

7.1. Is W1 a Dwarf Galaxy?

We now turn to the question of the nature of W1: is this object a dwarf galaxy or a star cluster? Due to its large mass-to-light ratio, observed metallicity spread, lack of mass segregation, and position on the size–luminosity plane, we conclude that W1 is a dwarf galaxy.

From our kinematic analysis (Section 4.1), we measure a mass-to-light ratio of 660 ± 590 from the 49 nonvariable member stars within 3 $r_{\rm half,ell}$. This large mass-to-light ratio, [illegible] unity indicate[illegible] matter-dominated object (e.g., N. F. Martin et al. 2007; J. D. Simon & M. Geha 2007). We [illegible] different half-light radii down to 2 $r_{\rm half,ell}$ does not change our results. For W1's stellar mass, [illegible]sistent with the larger Milky Way satellite galaxy population (M. Geha et al. 2026, see their Figure [illegible]) [illegible] metallicity analysis (Section 4.2), we find evidence for a metallicity spread ($\sigma_{\rm [Fe/H]} = 0.30^{+0.15}_{-0.11}$ dex) based on eight RGB stars with measured spectroscopic metallicities. This metallicity spread suggests that W1 has self-enriched, a property of satellites with dark matter halos that allow them to retain their gas more efficiently and go through successive epochs of star formation (e.g., B. Willman & J. Strader 2012; E. N. Kirby et al. 2013b).

We conduct a comprehensive search for the presence of mass segregation in W1 based on HST/ACS imaging (Section 5). We find a lack of mass segregation, which implies a dwarf galaxy classification and is consistent with previous work of H. Baumgardt et al. (2022). Recent simulations by R. Errani et al. (2025) suggest that mass segregation can occur in objects with very low stellar masses, even if they host a dark matter halo. However, W1's relatively large size and luminosity compared to the objects studied prolong its relaxation time beyond a Hubble time, making this effect negligible.

Finally, we compare the structural properties of W1 to other Milky Way satellites. We rely on the Local Volume Database of A. B. Pace (2025) for a comprehensive repository of the latest literature values of the observed properties of Milky Way dwarf galaxies, globular clusters, and ambiguous objects. The position of W1 on the size–luminosity plane of confirmed Milky Way satellites is more consistent with the dwarf galaxy population; W1 is significantly less compact than globular clusters with similar luminosities (see Figure 9, bottom panel).

Now, let's apply all that we
have learned about Willman
I to answer our two main
science questions!

(1) Is Willman 1 a dwarf galaxy or star cluster?

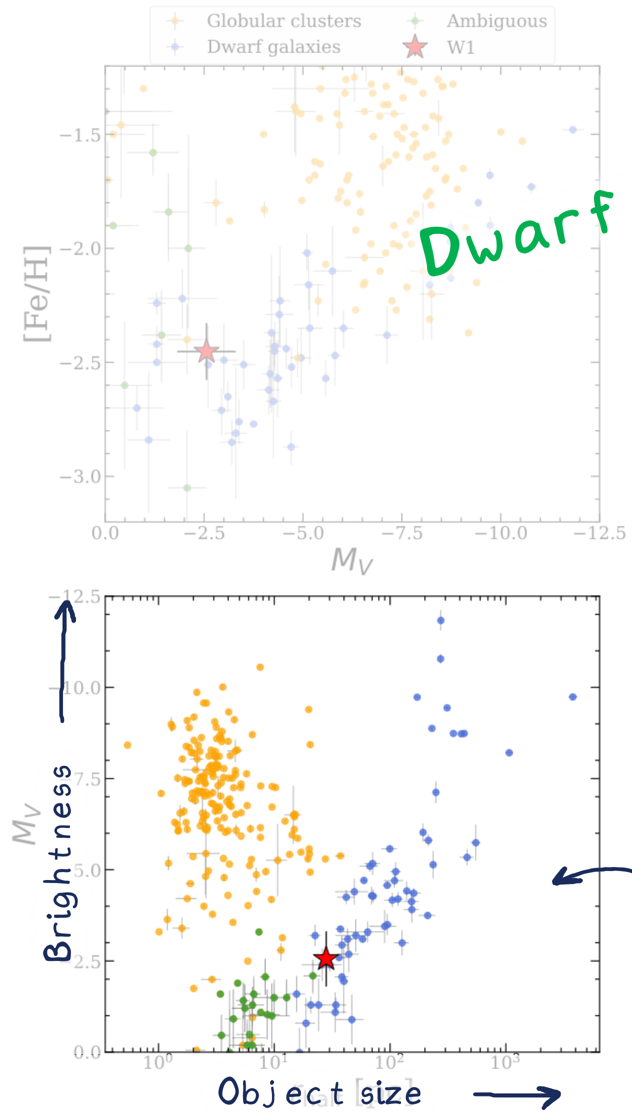

Figure 9. Comparison of W1 (red star) with other Milky Way dwarf galaxies (blue circles), globular clusters (orange circles), and ambiguous objects (green circles) taken from (A. B. Pace 2025). Top panel: [Fe/H] iron abundance spectroscopic metallicity as a function of absolute *V*-band magnitude. W1 is significantly fainter compared to other dwarf galaxies in its metallicity range, which could be explained by mass loss due to tidal stripping. Bottom panel: Absolute *V*-band magnitude vs. half-light radius. W1 is one of the faintest dwarf galaxies and has one of the smallest half-light radii.

Dwarf galaxy!!!

The size and brightness of Willman 1 (red star) are consistent with other dwarf galaxies (blue dots) and inconsistent with globular clusters (yellow dots).

7.2. Is W1 Tidally Disrupted?

The total mass of satellite systems is estimated under the assumption of dynamical equilibrium (J. Wolf et al. 2010). It is thus crucial to understand the dynamical state of W1 in order to determine whether its measured internal velocity dispersion is a true reflection of its dynamical mass. We will now weigh the evidence for and against tidal disruption.

The evidence for tidal disruption is as follows. First, the spatial distribution of W1 is elongated, with an ellipticity of $\epsilon = 0.47$ (R. R. Muñoz et al. 2018b). Crucially, high-probability member stars extend out to $3\,r_{\rm half,ell}$ and are not confined to only the central regions. Although we do not see the presence of extended spatial features beyond $3\,r_{\rm half,ell}$ (as suggested by previous work) and we report that the number density of stars is consistent with the expected Plummer distribution, this is not inconsistent with simulations of mildly stripped satellites (e.g., J. Peñarrubia et al. 2009).

Second, we continue to observe an irregular velocity profile, as originally noted in B. Willman et al. (2011), where the velocities of stars within $\sim 0.75\,r_{\rm half,ell}$ are systematically higher (see Figure 3, top panel). This produces a remarkably asymmetric, non-Gaussian velocity distribution (see Figure 4, bottom panel). Furthermore, we find that the velocity dispersion of the central member stars within $1\,r_{\rm half,ell}$ is significantly lower than the velocity dispersion measured out to $2\text{–}4\,r_{\rm half,ell}$, even when accounting for Milky Way interlopers via Gaussian mixture modeling.

The luminosity–metallicity relation has been shown to be tight for dwarf galaxies (E. N. Kirby et al. 2013b; J. D. Simon 2019; M. Geha et al. 2026). For satellites that initially conform to this relation, tidal stripping decreases their luminosity, while the average metallicity is unchanged. The location of satellites to the left of the luminosity–metallicity relation has been used as a diagnostic for tidal stripping (e.g., E. N. Kirby et al. 2013a, 2015; M. L. M. Collins et al. 2020; however, see A. H. Riley et al. 2026 for a more in-depth discussion). We find evidence for this phenomenon in the case of W1, where the luminosity of W1 is much fainter when compared to dwarf galaxies of similar metallicities (see Figure 9, top panel).

Our tidal-stream simulations for a W1-like progenitor show that W1's elongated structure is along the same axis as the high-density regions of the mock streams. These features are also aligned with the orbital trajectory of W1, consistent with the hypothesis that tidal stripping from the Milky Way's gravitational field could explain W1's elongated and elliptical spatial distribution.

Our best-fit orbital solutions conclusively predict W1 to currently be at apocenter, with a pericentric passage $\lesssim 25$ kpc. At this location, the Jacobi radius of W1 would be on the order of a few half-light radii, potentially allowing for the stripping of stars at the outskirts. We also compare the orbital parameters of W1 with those of other Milky Way dwarf galaxies and globular clusters in Figure 10. These parameters were determined by following the same methods as performed on W1 using the MW+LMC potential (Section 6.1). W1 has one of the smallest radial speeds and Galactocentric radii of the Milky Way's dwarf galaxies, consistent with a system with a high binding energy and early infall time (see Figure 10, center panel). In combination with its small pericenter and apocenter distances (see Figure 10, left panel), this suggests that slow tidal stripping from W1's sustained passage near the Milky Way over the course of its orbit could explain W1's elongated structural properties and irregular kinematic profile.

The evidence against tidal disruption is W1's large density, which implies that its half-light radius is smaller than its Jacobi radius (see Figure 10, right panel). However, we note multiple other dwarf galaxies with evidence for tidal disruption also lie above this line (e.g., Boötes I, Hercules; C. Filion & R. F. G. Wyse 2021; X. Ou et al. 2024). If W1 is indeed tidally disrupted and exhibits a large density, this could suggest that tidal stripping is more efficient than previously thought.

Overall, we find that the evidence for tidal disruption outweighs the evidence against it. The morphological and kinematic properties of W1 support a scenario in which W1

Star clusters vs. dwarf galaxies

• No dark matter	• Lotsss of dark matter ✓
• All stars have the same chemical composition	• Stars have different chemical compositions ✓
• Mass segregation	• No mass segregation ✓

(2) Is Willman I in dynamical equilibrium?

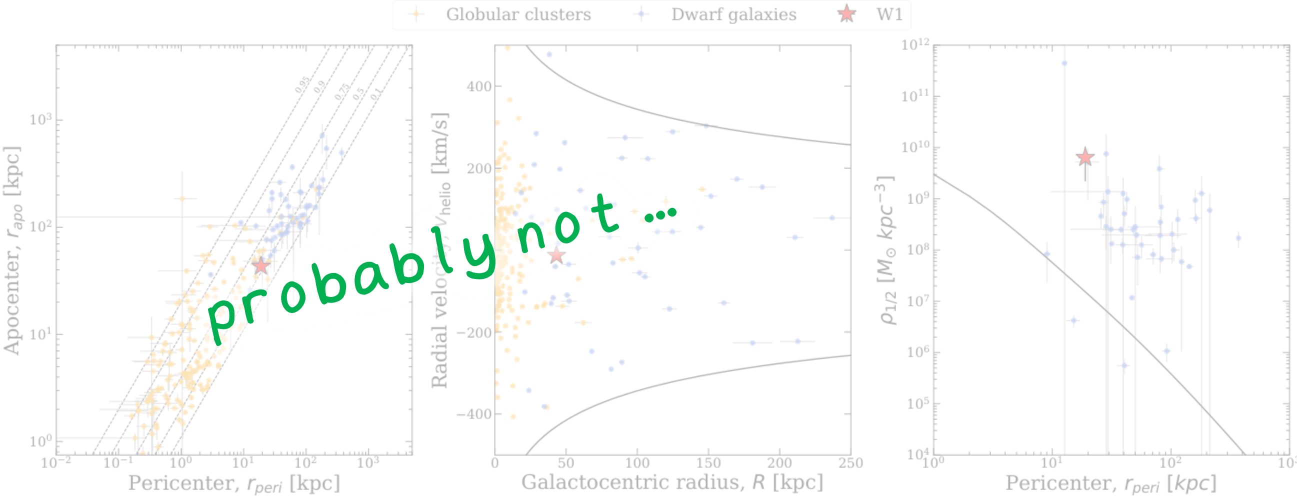

probably not ...

Figure 10. Comparison of the orbital properties of W1 with other Milky Way dwarf galaxies and globular clusters. W1 is denoted by a red star (see Table 2), Milky Way dwarf galaxies as blue circles, and globular clusters as orange circles (A. B. Pace 2025). Left panel: Apocenter distance as a function of pericenter distance. The locations of different orbital eccentricities are labeled as dotted lines. W1 has small pericenter and apocenter distances relative to other Milky Way dwarf galaxies. Center panel: Radial velocity as a function of Galactocentric radius, which corresponds to its binding energy and infall time (M. Rocha et al. 2012). The black lines represen[illegible] one of the smallest radial speeds and Galactocentric radii, corresponding to a high binding energy and early infall time (see Section 6.1). Right panel: Average density within one half-light rad[illegible] radius. According to A. B. Pace et al. (2022), if the satellite sits below this line, its Jacobi radius will be larger than the half-light radius, and it will likely be tidal disrupting.

Interactions with the Milky Way can stretch and pull apart small systems over time. Given its

- elongated shape,
- irregular velocity distribution, and
- orbit, which indicates a sustained passage near the Milky Way over the course of its orbit,

we conclude that Willman I is likely dynamically disturbed. This makes Willman I a promising candidate for testing the validity of dynamical equilibrium models on the smallest and faintest scales.

has experienced sustained tidal stripping due to its proximity to the Milky Way over the course of its orbit. Importantly, the presence of tidal stripping does not invalidate the evidence for W1's classification as a dwarf galaxy. Even if its current velocity dispersion is inflated or not fully representative of its dynamical mass, [illegible] spread, lack of mass segregation, and position on the size–luminosity plane [illegible] W1's dwarf galaxy classification. Therefore, while tidal effects may complicate the interpretation of the measured velocity dispersion, we still conclude that W1 is a dwarf galaxy that is likely tidally evolving with the Milky Way.

6. Conclusion

We have presented a comprehensive study of the structural, kinematic, chemical, and orbital properties of W1. Our main results are summarized as follows:

1. We identify a member sample of 56 stars, including six binaries, from new and improved Keck/DEIMOS spectroscopy and Gaia astrometry (Sections 2 and 3.1). We measure the physical properties of W1 from the 49 of these stars within 3 half-light radii.
2. We measure a systemic velocity of $v_{\rm sys} = -13.0^{+1.1}_{-1.1}$ km s^{-1} and a velocity dispersion of $\sigma_v = 4.7^{+1.5}_{-1.3}$ km s^{-1} based on a two-component Gaussian mixture model (Section 4.1). If W1 is in equilibrium, this implies a dynamical mass of $5.9^{+3.7}_{-3.4} \times 10^5\,M_\odot$ and a mass-to-light ratio of $(M/L)_V = 660 \pm 590$.
3. We measure an average metallicity of $[\rm Fe/H] = -2.45^{+0.12}_{-0.13}$ and metallicity dispersion $\sigma_{[\rm Fe/H]} = 0.30^{+0.15}_{-0.11}$ dex from eight member stars with CaT-based metallicity measurements (Section 4.2).
4. We conclude that W1 is a dwarf galaxy based on its dynamical mass-to-light ratio (Section 4.1), observed metallicity spread (Section 4.2), lack of mass segregation within $\sim 1\, r_{\rm half,ell}$ (Section 5.2), and position on the size–luminosity plane (Section 7.1).
5. Evidence for tidal disruption outweighs evidence against tidal disruption (Section 7.2). While W1 is quite dense, [illegible] (Section 6.1) and comparison with our simulations of tidal streams (Section 6.2) [illegible] passage near the Milky Way over the course of its orbit. This history could explain W1's elliptical shape, asymmetric velocity distribution (Section 4.1), and offset on the luminosity–metallicity plane.
6. We therefore caution that the internal velocity dispersion of W1 may not [illegible] reflect the dynamical mass of the system. The true dynamical nature of W1 may be [illegible] field imaging and spectroscopy as well as more detailed dynamical modeling to assess the [illegible] of equilibrium models.

Looking ahead, the upcoming Vera C. Rubin Observatory's Legacy Survey of Space and Time (LSST) is anticipated to uncover a population of similarly faint, distant, and low-luminosity Local Group satellites. Many of these objects are likely to resemble W1, with sparse red giant branches, uncertain membership, and properties that blur the line between star clusters and dwarf galaxies. Accurate characterization will require extensive spectroscopic follow-up in order to secure clean member samples, enabling precise kinematic and chemical measurements. By developing the tools needed to study these systems, we are better equipped to understand the satellites LSST will reveal and their place in the broader Local Group satellite population. From this, we can more comprehensively test the predictions of cosmological models and probe the processes that govern galaxy formation, evolution, and structure on the smallest scales.

We note that there is some evidence against this, specifically Willman I's high density! Maybe this means stars are stripped more efficiently than we thought?

Acknowledgments

We thank the anonymous referee for providing suggestions to our manuscript that improved its quality. We also thank Yasmeen Asali and Sebastian Monzon for their insightful comments. We thank Ricardo Muñoz for making his raw Megacam photometric catalogs available.

This research has made extensive use of the Keck Observatory Archive (KOA), which is operated by the W. M. Keck Observatory and the NASA Exoplanet Science Institute (NExScI), under contract with the National Aeronautics and Space Administration.

This work has made use of data from the European Space Agency (ESA) mission Gaia,[6] processed by the Gaia Data Processing and Analysis Consortium (DPAC[7]). Funding for the DPAC has been provided by national institutions, in particular the institutions participating in the Gaia Multilateral Agreement.

Facilities: Gaia, HST, Keck:II (DEIMOS).

Software: This research made use of many community-developed or community-maintained software packages, including (in alphabetical order): Astropy (Astropy Collaboration et al. 2013), Emcee (D. Foreman-Mackey et al. 2013), gala (A. M. Price-Whelan 2017), galpy (J. Bovy 2015), IPython (F. Perez & B. E. Granger 2007), Jupyter (jupyter.org), Matplotlib (J. D. Hunter 2007), NumPy (S. van der Walt et al. 2011), pandas (W. McKinney 2010), photutils (L. Bradley et al. 2025), and SciPy (E. Jones et al. 2001). This research has also made use of NASA's Astrophysics Data System.

All of the data we used are either archival data from the Keck II telescope or open access data from the Gaia satellite and the Hubble Space Telescope!

Astrophysics is built on open-source, community-developed software packages such as astropy!

Appendix
Details of Stars Used in Our Analysis

Table A1 present the properties of the 72 stars used in our analysis, including the 56 stars in our member sample (Section 3.2; $P_{\rm mem} > 0.5$) and the 65 stars used in our mixture model (Section 4.1; $P_{\rm mem,nov} > 0.1$, $r_{\rm half,ell} < 3$, Var $\neq 1$). We refer the reader to M. Geha et al. (2026) for a detailed discussion of the data reduction. The full table of stars, including nonmembers, is available in Table A3 of M. Geha et al. (2026).

Looking ahead, new wide-field surveys such as the Vera C. Rubin Observatory's Legacy Survey of Space and Time (LSST) will dramatically expand the population of known ultra-faint, distant, and compact satellites, allowing us to more comprehensively probe the extremes of galaxy formation, dynamical evolution, and structure.

---

[6] https://www.cosmos.esa.int/gaia

[7] https://www.cosmos.esa.int/web/gaia/dpac/consortium

Table A1
Measured Properties of Keck/DEIMOS Stars Used in Our Analysis

R.A. (deg)	Decl. (deg)	v (km s^{-1})	v_{err} (km s^{-1})	r_o (mag)	r_{err} (mag)	g_o (mag)	g_{err} (mag)	[Fe/H] …	[Fe/H]$_{err}$ (dex)	gaia_source_id …	Var …	P_{mem} …	Sample …
162.468917	51.061806	−19.51	0.69	18.045	0.020	18.632	0.020	−2.56	0.13	835977180433181056	0	0.68	1
162.325208	51.038000	−6.49	0.80	18.057	0.020	18.637	0.020	−2.31	0.13	835971820314006528	1	0.75	1
162.282500	50.947306	−11.87	1.37	18.294	0.020	18.218	0.020	…	…	835970136686823040	…	0.58	1
162.304708	51.042306	−24.46	3.03	19.790	0.020	19.429	0.020	…	…	836722438863176448	1	0.66	1
162.322625	51.057194	−11.87	1.16	19.997	0.020	20.445	0.020	−2.60	0.19	836722473222915968	0	0.81	1
162.366083	51.062861	−13.42	1.82	20.282	0.020	20.693	0.020	−2.62	0.22	835977725893619712	0	0.78	1
162.175708	51.033611	−6.48	1.33	20.364	0.020	20.595	0.020	…	…	836722889836066048	1	0.50	1
162.283708	51.040833	−9.97	0.97	20.429	0.020	20.905	0.020	−1.79	0.18	836722335783961216	0	0.90	1
162.292208	51.050083	−11.46	1.29	20.434	0.020	20.851	0.020	−2.72	0.19	836722404504886912	0	0.79	1
162.316583	51.040694	−9.50	2.24	20.471	0.021	20.925	0.020	−2.36	0.24	835971816018616320	0	0.62	1
162.338167	51.058389	−12.89	1.80	20.750	0.021	21.120	0.021	−2.85	0.30	835971854673199616	0	0.70	1
162.394000	51.044389	−64.30	1.96	20.766	0.021	21.224	0.021	…	…	835977416655970816	0	0.00	0
162.242208	51.048306	−6.74	1.77	20.795	0.021	21.321	0.022	…	…	836722198345008512	0	0.62	1
162.420125	51.061194	−15.91	1.75	20.891	0.025	21.198	0.023	…	…	835977588454665856	0	0.90	1
162.379000	51.061389	−15.15	2.88	20.903	0.021	21.227	0.021	…	…	835977691533881088	0	0.94	1
162.319833	51.067667	−17.51	2.14	20.915	0.021	21.276	0.021	…	…	836722546237412608	0	0.92	1
162.403417	51.064250	−10.79	3.05	20.998	0.021	21.216	0.021	…	…	835977588454666368	0	0.80	1
162.512042	51.042278	−13.00	2.47	21.184	0.021	21.598	0.021	…	…	…	0	0.62	1
162.379208	51.026111	−73.13	2.79	21.270	0.021	21.699	0.021	…	…	…	…	0.00	0
162.242000	51.089500	−98.13	3.04	21.330	0.024	21.859	0.029	…	…	…	0	0.00	0
162.366917	51.058194	−8.43	6.41	21.356	0.021	21.544	0.021	…	…	…	0	0.91	1
162.238083	51.042056	−12.68	3.64	21.395	0.022	21.631	0.021	…	…	…	0	1.00	1
162.366917	51.031000	−23.41	5.63	21.405	0.022	21.613	0.021	…	…	…	0	0.78	1
162.359708	51.054556	−8.05	2.75	21.425	0.022	21.654	0.021	…	…	…	0	0.95	1
162.302292	51.051500	−6.03	4.13	21.438	0.022	21.679	0.021	…	…	…	0	0.89	1
162.464708	51.031194	−21.26	2.85	21.482	0.022	21.866	0.021	…	…	…	0	0.46	0
162.354417	51.047889	0.50	3.96	21.484	0.021	21.729	0.021	…	…	…	0	0.64	1
162.281917	51.029500	−8.58	5.55	21.505	0.022	21.732	0.021	…	…	…	0	0.91	1
162.394917	51.074583	−18.42	4.47	21.512	0.022	21.798	0.021	…	…	…	0	0.79	1
162.185083	51.035028	−8.09	3.40	21.521	0.022	21.770	0.021	…	…	…	1	0.90	1
162.264208	51.013500	−3.26	7.06	21.544	0.022	21.649	0.021	…	…	…	…	0.66	1
162.373917	51.049500	−19.65	4.41	21.586	0.022	21.784	0.021	…	…	…	0	0.88	1
162.291417	51.015611	−6.23	6.02	21.625	0.022	21.820	0.021	…	…	…	0	0.83	1
162.296750	51.075083	−9.78	3.27	21.638	0.022	21.865	0.021	…	…	…	0	0.91	1
162.447375	51.059639	−7.81	6.17	21.658	0.022	21.933	0.021	…	…	…	0	0.84	1
162.365208	51.059111	−11.66	4.76	21.676	0.022	21.901	0.021	…	…	…	0	0.98	1
162.354333	51.040333	−14.41	4.94	21.702	0.022	21.932	0.021	…	…	…	0	0.98	1
162.325250	51.054694	−3.68	10.09	21.715	0.023	21.842	0.021	…	…	…	…	0.75	1
162.203083	51.054694	63.33	5.23	21.751	0.022	22.223	0.022	…	…	…	…	0.00	0
162.271500	51.028389	−9.53	4.68	21.771	0.023	21.941	0.021	…	…	…	…	0.93	1
162.340083	51.045917	−8.79	6.32	21.798	0.023	22.021	0.022	…	…	…	1	0.90	1
162.323292	51.045389	−18.42	5.28	21.818	0.023	22.046	0.022	…	…	…	0	0.90	1
162.412500	51.082611	−11.91	11.86	21.832	0.023	22.095	0.023	…	…	…	…	0.93	1
162.321028	51.072971	−21.50	13.57	21.916	0.023	22.209	0.022	…	…	…	…	0.73	1
162.339500	51.042889	−6.48	10.91	22.000	0.023	22.209	0.022	…	…	…	…	0.94	1
162.307500	51.006306	24.23	7.34	22.090	0.023	22.368	0.022	…	…	…	…	0.07	0
162.316875	51.049889	−13.64	7.03	22.110	0.024	22.314	0.022	…	…	…	…	0.99	1

In the interest of reproducibility, we include the data for all the stars used in our analysis. The full data for all the Milky Way satellites observed with Keck/DEIMOS can be accessed here!

Congratulations on making it to the end of this paper! Feel free to reach out to camille.chiu@yale.edu with any questions :)

This accessible “paper doodle” was inspired by the work of Dr. Claire Lamman. You should check out her research, her annotated papers, and the full collection of paper doodles! This paper was annotated using the beautiful XKCD font.

Thank you again for reading about my research. I hope you enjoyed and learned something new about dwarf galaxies!!

You can read more about my research on my website: https://camchiu.github.io/ 🌱

You can read more about the full data on the Geha Group website: https://geha-group.github.io/deimos/

Until the next doodle,

Camille Chiu

Table A1
(Continued)

R.A. (deg)	Decl. (deg)	v (km s^{-1})	v_{err} (km s^{-1})	[illegible] (mag)	[illegible] (mag)	[illegible] (mag)	g_{err} (mag)	[Fe/H] …	$[Fe/H]_{err}$ (dex)	gaia_source_id …	Var	P_{mem} …	Sample …
162.362833	51.058361	−9.94	14.21	[illegible]	[illegible]	[illegible]	0.023	[illegible]	[illegible]	…	[illegible]	[illegible]	1
162.348625	51.051083	7.51	[illegible]	[illegible]	[illegible]	[illegible]	0.023	[illegible]	[illegible]	…	[illegible]	[illegible]	0
162.315500	51.022611	−29.34	5.03	[illegible]	[illegible]	[illegible]	0.023	[illegible]	[illegible]	…	[illegible]	[illegible]	0
162.261708	50.994500	[illegible]	[illegible]	22.164	[illegible]	[illegible]	0.023	[illegible]	[illegible]	…	[illegible]	[illegible]	1
162.450625	51.030111	[illegible]	[illegible]	[illegible]	[illegible]	[illegible]	0.023	[illegible]	[illegible]	…	[illegible]	[illegible]	1
162.481266	51.063726	[illegible]	[illegible]	[illegible]	[illegible]	[illegible]	0.024	[illegible]	[illegible]	…	[illegible]	[illegible]	1
162.312208	51.048306	[illegible]	[illegible]	[illegible]	0.026	22.610	0.024	[illegible]	[illegible]	…	[illegible]	[illegible]	1
162.191875	51.000000	[illegible]	[illegible]	22.364	[illegible]	[illegible]	0.023	[illegible]	[illegible]	…	[illegible]	[illegible]	0
162.328792	51.081500	[illegible]	[illegible]	[illegible]	[illegible]	[illegible]	0.024	[illegible]	[illegible]	…	[illegible]	[illegible]	1
162.306000	51.045389	[illegible]	6.82	[illegible]	0.026	[illegible]	0.024	[illegible]	[illegible]	…	[illegible]	[illegible]	1
162.386417	51.074194	[illegible]	7.54	[illegible]	[illegible]	[illegible]	0.024	[illegible]	[illegible]	…	[illegible]	[illegible]	1
162.440208	51.035806	[illegible]	6.94	[illegible]	[illegible]	[illegible]	0.024	[illegible]	[illegible]	…	[illegible]	[illegible]	1
162.448375	51.034389	[illegible]	10.24	[illegible]	[illegible]	[illegible]	0.025	[illegible]	[illegible]	…	[illegible]	[illegible]	1
162.295375	51.037194	[illegible]	[illegible]	[illegible]	[illegible]	[illegible]	0.025	[illegible]	[illegible]	…	[illegible]	[illegible]	1
162.364917	51.033611	[illegible]	6.73	22.615	[illegible]	[illegible]	0.025	[illegible]	[illegible]	…	[illegible]	[illegible]	0
162.341583	51.055000	[illegible]	[illegible]	22.640	0.028	[illegible]	0.025	[illegible]	[illegible]	…	[illegible]	[illegible]	0
162.292417	51.082694	[illegible]	10.37	22.752	[illegible]	[illegible]	0.029	[illegible]	[illegible]	…	[illegible]	[illegible]	0
162.434917	51.050694	[illegible]	[illegible]	22.774	[illegible]	[illegible]	0.026	[illegible]	[illegible]	…	[illegible]	[illegible]	1
162.281203	51.055597	[illegible]	[illegible]	[illegible]	[illegible]	[illegible]	0.027	[illegible]	[illegible]	…	[illegible]	[illegible]	0
162.373000	51.062611	[illegible]	[illegible]	[illegible]	0.032	[illegible]	0.028	[illegible]	[illegible]	…	[illegible]	[illegible]	0
162.269708	51.054611	[illegible]	6.03	[illegible]	[illegible]	[illegible]	0.026	[illegible]	[illegible]	…	[illegible]	[illegible]	1
162.326000	51.059500	[illegible]	[illegible]	[illegible]	[illegible]	[illegible]	0.027	[illegible]	[illegible]	…	[illegible]	[illegible]	1
162.227000	51.057889	[illegible]	[illegible]	[illegible]	[illegible]	[illegible]	0.030	[illegible]	[illegible]	…	[illegible]	[illegible]	1
162.496000	51.048806	[illegible]	6.15	[illegible]	[illegible]	[illegible]	0.030	[illegible]	[illegible]	…	[illegible]	[illegible]	0
162.216547	51.040881	29.80	8.04	[illegible]	[illegible]	[illegible]	0.035	[illegible]	[illegible]	…	[illegible]	[illegible]	0

(This table is available in its entirety in machine-readable form in the online article.)

ORCID iDs

Camille Chiu https://orcid.org/0000-0001-5915-4264
Marla Geha https://orcid.org/0000-0002-7007-9725
William Cerny https://orcid.org/0000-0003-1697-7062
Nitya Kallivayalil https://orcid.org/0000-0002-3204-1742
Hannah Richstein https://orcid.org/0000-0002-3188-2718
Christopher T. Garling https://orcid.org/0000-0001-9061-1697
Beth Willman https://orcid.org/0000-0003-2892-9906

References

Aliu, E., et al. 2009, ApJ, 697, 1299
Armstrong, B. M., Bekki, K., & Ludlow, A. D. 2021, MNRAS, 500, 2937
Astropy Collaboration, et al. 2013, A&A, 558, A33
Battaglia, G., & Starkenburg, E. 2012, A&A, 539, A123
Baumgardt, H., Faller, J., Meinhold, N., McGovern-Greco, C., & Hilker, M. 2022, MNRAS, 510, 3531
Belokurov, V., et al. 2007, ApJ, 654, 897
Binney, J., & Tremaine, S. 2008, Galactic Dynamics (2nd Edition; Princeton Univ. Press)
Bovy, J. 2015, ApJS, 216, 29
Bradley, L., et al. 2025, astropy/photutils: 2.2.0, v2.2.0 Zenodo, doi:10.5281/zenodo.14889440
Bressan, A., Marigo, P., Girardi, L., et al. 2012, MNRAS, 427, 127
Bringmann, T., Doro, M., & Fornasa, M. 2009, JCAP, 2009, 016
Carrera, R., Pancino, E., Gallart, C., & del Pino, A. 2013, MNRAS, 434, 1681
Cerny, W., et al. 2025, ApJ, 979, 164
Choi, J., Dotter, A., Conroy, C., et al. 2016, ApJ, 823, 102
Collins, M. L. M., Tollerud, E. J., Rich, R. M., et al. 2020, MNRAS, 491, 3496
Correa Magnus, L., & Vasiliev, E. 2022, MNRAS, 511, 2610
D'Souza, R., & Bell, E. F. 2022, MNRAS, 512, 739
Dey, A., et al. 2019, AJ, 157, 168
Dotter, A. 2016, ApJS, 222, 8
Drlica-Wagner, A., et al. 2015, ApJ, 813, 109
Durbin, M. J., et al. 2025, ApJ, 992, 106
Erkal, D., et al. 2021, MNRAS, 506, 2677
Errani, R., Peñarrubia, J., & Walker, M. G. 2025, ApJ, 993, 160
Faber, S. M. 2003, SPIE, 4841, 1657
Fardal, M. A., Huang, S., & Weinberg, M. D. 2015, MNRAS, 452, 301
Filion, C., & Wyse, R. F. G. 2021, ApJ, 923, 218
Ford, H. C., et al. 1998, SPIE, 3356, 234
Foreman-Mackey, D., Hogg, D. W., Lang, D., & Goodman, J. 2013, PASP, 125, 306
Fritz, T. K., Battaglia, G., Pawlowski, M. S., et al. 2018, A&A, 619, A103
Fu, S. W., et al. 2023, ApJ, 958, 167
Gaia Collaboration, et al. 2023, A&A, 674, A1
Geha, M., Pelliccia, D., Prochaska, J. X., et al. 2026, ApJ, 999, 140
Gullikson, K., Dodson-Robinson, S., & Kraus, A. 2014, AJ, 148, 53
Hernquist, L. 1990, ApJ, 356, 359
Hinton, S. R., Davis, T. M., Lidman, C., Glazebrook, K., & Lewis, G. F. 2016, A&C, 15, 61
Homma, D., et al. 2024, PASJ, 76, 733
Hunter, J. D. 2007, CSE, 9, 90
Husser, T. O., Wende-von Berg, S., Dreizler, S., et al. 2013, A&A, 553, A6
Innanen, K. A., Harris, W. E., & Webbink, R. F. 1983, AJ, 88, 338
Ji, A. P., et al. 2021, ApJ, 921, 32
Jones, E., Oliphant, T., Peterson, P., et al. 2001, SciPy: Open source scientific tools for Python, www.scipy.org
Kim, D., Jerjen, H., Milone, A. P., Mackey, D., & Da Costa, G. S. 2015, ApJ, 803, 63
Kirby, E. N., Boylan-Kolchin, M., Cohen, J. G., et al. 2013a, ApJ, 770, 16
Kirby, E. N., Cohen, J. G., Guhathakurta, P., et al. 2013b, ApJ, 779, 102
Kirby, E. N., Cohen, J. G., Simon, J. D., & Guhathakurta, P. 2015, ApJL, 814, L7
Koposov, S. E., Belokurov, V., Torrealba, G., & Evans, N. W. 2015, ApJ, 805, 130
Li, S., Liang, Y.-F., & Fan, Y.-Z. 2021, PhRvD, 104, 083037
Loewenstein, M., & Kusenko, A. 2010, ApJ, 714, 652
Loewenstein, M., & Kusenko, A. 2012, ApJ, 751, 82
Longeard, N., et al. 2018, MNRAS, 480, 2609
Machado, R. E. G., Tauil, G. C., & Schweder-Souza, N. 2025, Univ, 11, 191
Martin, N. F., Ibata, R. A., Chapman, S. C., Irwin, M., & Lewis, G. F. 2007, MNRAS, 380, 281
Martin, N. F., de Jong, J. T. A., & Rix, H.-W. 2008, ApJ, 684, 1075
Martinez, G. D., Minor, Q. E., Bullock, J., et al. 2011, ApJ, 738, 55
Maxted, P. F. L., Heber, U., Marsh, T. R., & North, R. C. 2001, MNRAS, 326, 1391
McDaniel, A., Ajello, M., Karwin, C. M., et al. 2024, PhRvD, 109, 063024
McKinney, W. 2010, in Proc. of the 9th Python in Science Conf., ed. S. van der Walt & J. Millman (SciPy), 51
Miyamoto, M., & Nagai, R. 1975, PASJ, 27, 533
Muñoz, R. R., Côté, P., Santana, F. A., et al. 2018a, ApJ, 860, 65
Muñoz, R. R., Côté, P., Santana, F. A., et al. 2018b, ApJ, 860, 66
Navabi, M., Carrera, R., Noël, N. E. D., et al. 2026, MNRAS, 546, stag019
Navarro, J. F., Frenk, C. S., & White, S. D. M. 1997, ApJ, 490, 493
Nieto, D., & Mirabal, N. 2010, arXiv:1003.3745
Ou, X., et al. 2024, ApJ, 966, 33
Pace, A. B. 2025, OJAp, 8, 142
Pace, A. B., Erkal, D., & Li, T. S. 2022, ApJ, 940, 136
Patel, E., Chatur, R., & Mao, Y.-Y. 2024, ApJ, 976, 171
Paust, N. E. Q., et al. 2009, AJ, 137, 246
Peñarrubia, J., Navarro, J. F., McConnachie, A. W., & Martin, N. F. 2009, ApJ, 698, 222
Perez, F., & Granger, B. E. 2007, CSE, 9, 21
Plummer, H. C. 1911, MNRAS, 71, 460
Price-Whelan, A. M. 2017, JOSS, 2, 388
Prochaska, J. X., Hennawi, J. F., Westfall, K. B., et al. 2020, JOSS, 5, 2308
Richstein, H., et al. 2024, ApJ, 967, 72
Riley, A. H., et al. 2026, MNRAS, 546, stag029
Rocha, M., Peter, A. H. G., & Bullock, J. 2012, MNRAS, 425, 231
Saeedi, S., & Sasaki, M. 2020, MNRAS, 499, 3111
Schiavon, R. P., Barbuy, B., Rossi, S. C. F., & Milone, A. 1997, ApJ, 479, 902
Schlegel, D. J., Finkbeiner, D. P., & Davis, M. 1998, ApJ, 500, 525
Siegel, M. H., Shetrone, M. D., & Irwin, M. 2008, AJ, 135, 2084
Simon, J. D. 2018, ApJ, 863, 89
Simon, J. D. 2019, ARA&A, 57, 375
Simon, J. D., & Geha, M. 2007, ApJ, 670, 313
Sirianni, M., et al. 2005, PASP, 117, 1049
Smith, S. E. T., et al. 2024, ApJ, 961, 92
Sohn, S. T., et al. 2007, ApJ, 663, 960
Stetson, P. B. 1987, PASP, 99, 191
Stetson, P. B. 1992, ASPC, 25, 297
Torrealba, G., et al. 2016, MNRAS, 463, 712
Tripathi, A., Panwar, N., Sharma, S., Kumar, B., & Rastogi, S. 2023, JApA, 44, 61
Walker, M. G., Mateo, M., Olszewski, E. W., et al. 2006, AJ, 131, 2114
Weatherford, N. C., Chatterjee, S., Kremer, K., & Rasio, F. A. 2020, ApJ, 898, 162
Willman, B., & Strader, J. 2012, AJ, 144, 76
Willman, B., et al. 2005, AJ, 129, 2692
Willman, B., et al. 2006, arXiv:astro-ph/0603486
Willman, B., Geha, M., Strader, J., et al. 2011, AJ, 142, 128
Wolf, J., Martinez, G. D., Bullock, J. S., et al. 2010, MNRAS, 406, 1220
van der Marel, R. P., & Kallivayalil, N. 2014, ApJ, 781, 121
van der Walt, S., Colbert, S. C., & Varoquaux, G. 2011, CSE, 13, 22

Unlike other fields where the final scientific product may be something physical (vaccine, rocket, new molecule, etc.), all modern astrophysics knowledge is preserved in scientific papers, plots, and tables. This is how astrophysicists document, share, and inspire the work of others.

This research would not be possible without the time, dedication, and ideas of so many others before us!

The original discovery paper for Willman 1, over 20 years ago!

<u>Fun fact:</u> Besides the Large and Small Magellanic Clouds, Willman 1 is the only other Milky Way dwarf galaxy (now confirmed!) named after a person.